

Reconfiguring colours of single relief structures by directional stretching

Qifeng Ruan,^{1,2} Wang Zhang,² Hao Wang,² John You En Chan,² Hongtao Wang,^{2,3} Hailong Liu,⁴

Dianyuan Fan,¹ Ying Li,^{1,*} Cheng-Wei Qiu,^{3,*} Joel K.W. Yang^{2,4,*}

¹SZU-NUS Collaborative Innovation Center for Optoelectronic Science & Technology, International Collaborative Laboratory of 2D Materials for Optoelectronics Science and Technology of Ministry of Education, Institute of Microscale Optoelectronics, Shenzhen University, Shenzhen 518060, China

²Engineering Product Development Pillar, Singapore University of Technology and Design, 8 Somapah Road, Singapore 487372, Singapore

³Singapore Department of Electrical and Computer Engineering, National University of Singapore, Singapore 117583, Singapore

*⁴Institute of Materials Research and Engineering, A*STAR (Agency for Science, Technology and Research), Singapore 138634, Singapore*

*queenly@szu.edu.cn; chengwei.qiu@nus.edu.sg; joel_yang@sutd.edu.sg

Abstract

Colour changes can be achieved by straining photonic crystals or gratings embedded in stretchable materials. However, the multiple repeat units and the need for a volumetric assembly of nanostructures limit the density of information content. Inspired by surface reliefs on oracle bones and music records as means of information archival, here we endow surface-relief elastomers with multiple sets of information that are accessible by mechanical straining along in-plane axes. Distinct from Bragg diffraction effects from periodic structures, we report trenches that generate colour due to variations in trench depth, enabling individual trench segments to support a single colour. Using 3D printed cuboids, we replicated trenches of varying geometric parameters in elastomers. These parameters determine the initial colour (or lack thereof), the response to capillary forces, and the appearance when strained along or across the trenches. Strain induces modulation in trench depth or the opening and closure of a trench, resulting in surface reliefs with up to six distinct states, and an initially featureless surface that reveals two distinct images when stretched along different axes. The highly reversible structural colours are promising in optical data archival, anti-counterfeiting, and strain-sensing applications.

Keywords: structural colours, reliefs, elastomers, security prints

Surface reliefs have been effective in storing tactile, visual, analogue and digital information with many fascinating examples: Engraved reliefs of early text and art on oracle bones¹ and stones, such as the Rosetta Stone², record the lives of the ancients; coins possess ridges or grooves on the edges as a heritage of Isaac Newton's 17th century solution to avoid illegal clipping of precious metal coins and counterfeiting³; vinyl records and compact discs rely on reliefs to store high-density audio and digital

music⁴. Thus, reliefs have proven effective as a media for recording, displaying and storing information. However, they are rigid, static, and hence lack the ability to exhibit multiple sets of information.

Colour information encoded by the geometry of materials, instead of their chemical compositions, is known as physical or structural colours. Structural colours arising from light interference in thin films⁵/cavities⁶/concave interfaces⁷, diffraction effects in photonics crystals⁸, light scattering/absorption in plasmonic materials^{9,10}, as well as Mie resonances in high-refractive-index nanostructures^{11,12}, have been discovered. Compared to pigments and dyes, structural colours are potentially fade-resistant and possess unprecedented print resolution¹³⁻¹⁶. Reversible tuning of structural colours can be achieved by various external stimuli, including but not limited to gases¹⁷, solvents¹⁸, light¹⁹, temperature changes²⁰, voltage biases^{21,22}, magnetic fields^{23,24}, and mechanical forces^{25,26}. Flexible elastomers, especially inert, optical transparent, and biological compatible polydimethylsiloxane (PDMS)²⁷⁻²⁹, are excellent materials for realizing reversible mechanochromic effects. Elastomers have been used as substrates/matrices for supporting/embedding periodical arrays of uniform plasmonic nanocuboids³⁰, titania nanoblocks³¹, silica nanospheres^{32,33}, and air nanocylinders^{34,35}. Once the elastomers are stretched, the lattice constants are changed and lead to colour variations. However, less attention has been paid to colour shifts due to the shape deformation of the individual constituent structures. Individual structures with reconfigurable colours could lead to microprints with higher information density and strain sensors with a simpler implementation.

Here, we report a new mechanism for reversibly switching multiple-state structural colours of flexible reliefs by directional strains and capillary forces. PDMS reliefs with cuboid trenches were moulded from templates fabricated using two-photon polymerization lithography (TPL). Compared with bottom-up self-assembly approach and 2D photo/electron-beam lithography, TPL based nanoscale

3D printing provides greater design freedom to define structures in all dimensions. Cuboids with different heights can therefore be printed in a single lithographic step. The transmitted colours through the PDMS trenches were analysed both by diffraction theory and from the perspective of single-trench scattering. With the assistance of mechanical and electromagnetic simulations, shifts in the colours induced by stretching resulted predominantly from the depth transformation of the trenches. Surprisingly, hue is not significantly affected by the periodicity of the patterns, unlike conventional Bragg-diffraction based structural colours³²⁻³⁵. As an additional variation, capillary forces collapse the trenches and scramble the appearance of the prints, while directional strains selectively recover the structures into the upright position, resetting the colours. Though deterministic capillary-force-induced collapse of high-aspect-ratio structures has been reported³⁶⁻³⁸, few approaches can overcome van der Waals forces to achieve structure recovery. An elastomer relief with microtrenches was accordingly designed and exhibited six states of colour microprints. We further pushed the dimension of trenches to the nanoscale to achieve surface reliefs that exhibit a featureless initial state. With pixel-by-pixel positioning of cross trenches of suitable depths, these featureless nanoreliefs reveals two distinct colourful images when strained along different axes. The mechanochromic effects of the monolithic reliefs were found to be highly reproducible even after 200 stretching/releasing cycles. Our results highlight the potential applications of soft reliefs in strain sensors, security prints, and active colour filters.

Results and discussion

PDMS reliefs with multiple states of colour images (Fig. 1a) were designed using trenches (Fig. 1b) as building blocks. Strain modulation (green arrows in Fig. 1a, b), capillary-force-caused collapse

(blue arrows), and directional-strain-induced recovery (orange arrows) of the PDMS trenches were adopted to display multiple colour information. PDMS reliefs with cuboid trenches of different lengths, widths, and depths were moulded from 3D printed polymer templates (Supplementary Fig. 1). A negative photoresist IP-Dip was cured by a focused femtosecond laser to form cuboids in a TPL system. The IP-Dip cuboids were printed layer by layer with a slicing distance of 0.2 μm . To print each layer, the laser beam was line-scanned along the length direction of each cuboid with a hatching distance of 0.1 μm between the adjacent lines. Fig. 1c shows a scanning electron microscope (SEM) image of a representative IP-Dip cuboid array. Each cuboid with a width of 1.55 μm was printed by scanning 13 adjacent lines for each layer. The cuboid array was used as the template to fabricate PDMS slabs patterned with the inverse structures (Fig. 1d).

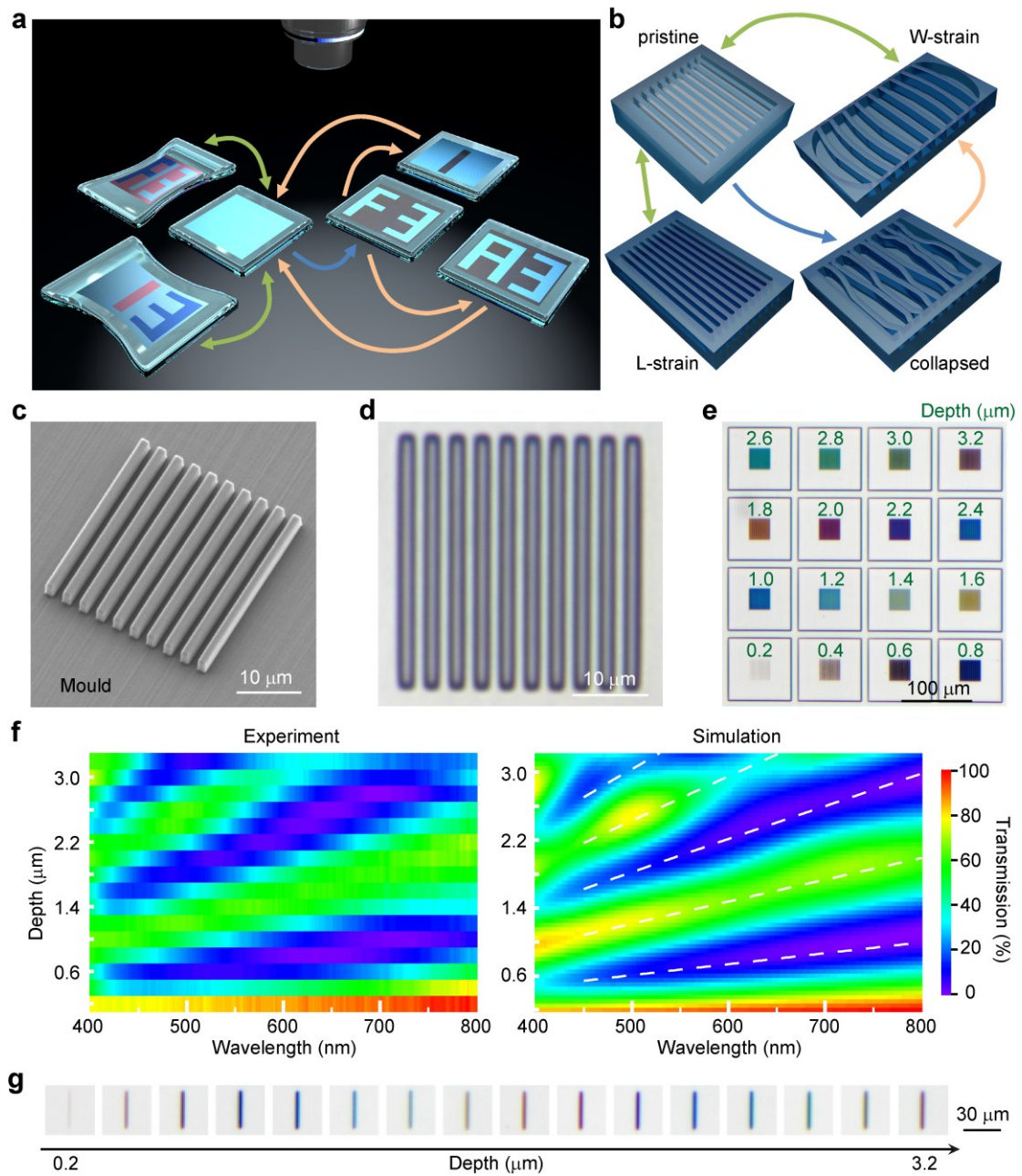


Fig. 1 | Colourful PDMS reliefs. **a**, Schematic of PDMS relief with multiple states of colour images revealed by directional strains and capillary force. **b**, 3D schematic of the PDMS trenches (pristine), stretched trenches with strains along the length (L-strain) and width (W-strain) directions, as well as capillary force-collapsed trenches. The green, blue, and orange arrows represent strain modulation, capillary-force-caused collapse, and directional-strain-induced recovery, respectively. **c**, 30° tilted view scanning electron micrograph of a representative cuboid mould printed in IP-Dip. The cuboid array has a length of 30 μm, width of 1.55 μm, height of 2.8 μm, and pitch of 3 μm. **d**, High-magnified optical

image of the PDMS trenches replica-moulded from the IP-Dip cuboid array in (c), captured using a 50× objective with a 0.4 numerical aperture (NA) in reflection mode. **e**, Transmission optical micrograph of PDMS trench arrays with varying depths as indicated with fixed length of 30 μm, width of 1.55 μm, and pitch of 3 μm. **f**, Measured and simulated transmittance spectra of the PDMS trenches in (e) obtained with unpolarized incident light. White dash lines indicate analytical functions of depth-dependent dip and peak wavelengths based on Kirchhoff's scalar wave approximation. **g**, Transmission optical micrograph of individual PDMS trenches with a fixed length of 30 μm, width of 1.55 μm, and varying depths. Transmission images and spectra are obtained using a 5×, 0.15 NA objective.

The obtained PDMS trenches with varying depths exhibit rich colours when observed under an optical microscope (Fig. 1e). The transmission spectra of the colourful PDMS trenches were recorded using a 5× objective. The depth-dependent transmission spectra using finite-difference time-domain (FDTD) based full-vectorial electromagnetic simulations show excellent agreement with experiments (Fig. 1f). To obtain an intuitive physical insight into the origin of peaks and valleys in the transmission spectra, we applied Kirchhoff's scalar wave approximation^{39,40}. The PDMS trenches were approximated as a binary phase grating with a phase difference of

$$\Delta\varphi = \frac{2\pi d(n_{\text{PDMS}} - n_{\text{air}})}{\lambda} \quad (1)$$

where d is the depth of the trenches, n_{PDMS} and n_{air} are the refractive indices of PDMS and air, respectively. Once the phase difference equals an odd (even) integer number of π , the zero-order diffraction reaches its minimum (maximum) intensity. The peak and dip wavelengths were therefore estimated to be

$$\lambda = \frac{2(n_{\text{PDMS}} - n_{\text{air}})}{i} d \quad (2)$$

where integral multiples (i) of half-wavelengths match the difference in the optical path length between light travelling through the PDMS ridge and air trench. For $i = 1$ to 5, the depth-dependent dips and peaks of the zero-order diffraction are plotted in the wavelength region of 450 – 800 nm (dash lines in Fig. 1f). Considering the pitch (3 μm) of the PDMS trenches and the NA (0.15) of the objective, the transmitted light with wavelengths larger than 450 nm solely contains the zero-order diffraction without contribution from high-order diffraction. Some contribution from the first-order diffraction is collected for wavelengths smaller than 450 nm.

In contrast to the polarization-independent diffraction of the scalar description³⁹, a slight difference exists between the FDTD simulated transmission spectra for light polarized along the length and width directions of the PDMS trenches (Supplementary Fig. 2a). A 22 nm difference in transmission peak wavelength was obtained for the two polarizations. Although Kirchhoff's scalar wave theory is expected to be accurate only for coarse and shallow gratings³⁹, here it serves reasonably well as an intuitive guide to understanding the trends in the depth-dependent transmission spectra.

IP-Dip cuboids with fixed heights but varied widths and pitches were also printed in a single step to replica-mould PDMS trench arrays (Supplementary Fig. 3). For fixed heights of 2.8 μm and pitches of 3 μm , the IP-Dip cuboids with widths smaller than 0.7 μm or larger than 2.1 μm produced unstable PDMS trenches during the demoulding process, as either the distances between adjacent PDMS ridges are too small or the PDMS ridges are too thin. Similarly, stable PDMS trench arrays with fixed widths of 1.55 μm and depths of 2.8 μm could not be obtained unless the designed pitch is larger than 2.6 μm . PDMS trench arrays with different saturation were achieved by varying the width and pitch, while the hue is more sensitive to the depth.

Remarkably, even a single PDMS trench can produce a colour similar to the PDMS trench arrays (Fig. 1g, Supplementary Fig. 2). Considering that bulk PDMS is highly transmissive to visible light, the colour could be ascribed to the scattering loss of light propagating outside the 8.6° half-angle collection cone of the objective. FDTD simulations showed that the forward scattering of the PDMS trench with a light deviation angle in the range of $8.6^\circ - 90^\circ$ dominates the scattering loss (Supplementary Fig. 2e). For incident light polarized along either the length or width directions of the trench, the forward scattering peak (valley) wavelengths of the single PDMS trench are close to the transmission valley (peak) wavelengths of the trench array. This effect makes it possible to design and fabricate microprints with colour pixels at the single trench level.

The outstanding stretchability of PDMS enables the modulation of the shapes and structural colours of the reliefs. When strains along the length direction of the PDMS trenches were applied, both the shape and transmission colour of the trench arrays were changed (Fig. 2a). Taking the 2.8- μm -depth trench array as an example, the colour gradually shifts from green to blue, purple, and dark khaki, with the increasing L-strain from 0 to 0.8. In contrast, no obvious hue variation but a decrease in saturation was observed when strained along the width of the trenches. The deformed shapes of a representative trench array were captured by a $50\times$ objective in reflection mode (Fig. 2b).

To model the hyperelastic PDMS, the strain-stress relationship measured in the uniaxial tensile test (Supplementary Fig. 4) was fitted by an incompressible Mooney-Rivlin model⁴¹. The strain-induced deformations of PDMS trenches were then simulated using 3D finite-element analysis. The simulated shape deformations under different strains (Fig. 2c) are in excellent agreement with the experimental results (Fig. 2b). The depth of the PDMS trenches (Supplementary Fig. 5, Supplementary Table 1) dramatically decreases from 2.8 to 2.51, 2.31, 2.14 and 1.92 μm with the L-strain increasing

from 0 to 0.2, 0.4, 0.6 and 0.8, accounting for the substantial blueshift of the transmission spectra (Fig. 2d). On the other hand, W-strain only slightly deepens the trenches, but significantly increases the distance between adjacent PDMS ridges. Slight redshifts and reduced peak-to-valley ratios on the transmission spectra were therefore observed both in the experiment and FDTD simulations (Fig. 2d). Note that the maximum von Mises stress in the stretched PDMS trenches is less than 3 MPa (Supplementary Fig. 6), the local stress-induced refractive index change⁴² of PDMS in the order of 10^{-3} is neglected in the FDTD simulations. All colours completely recover to the initial states once the strain is released. Moreover, the colour changes are reversible during multiple stretching/releasing cycles (Supplementary Fig. 7).

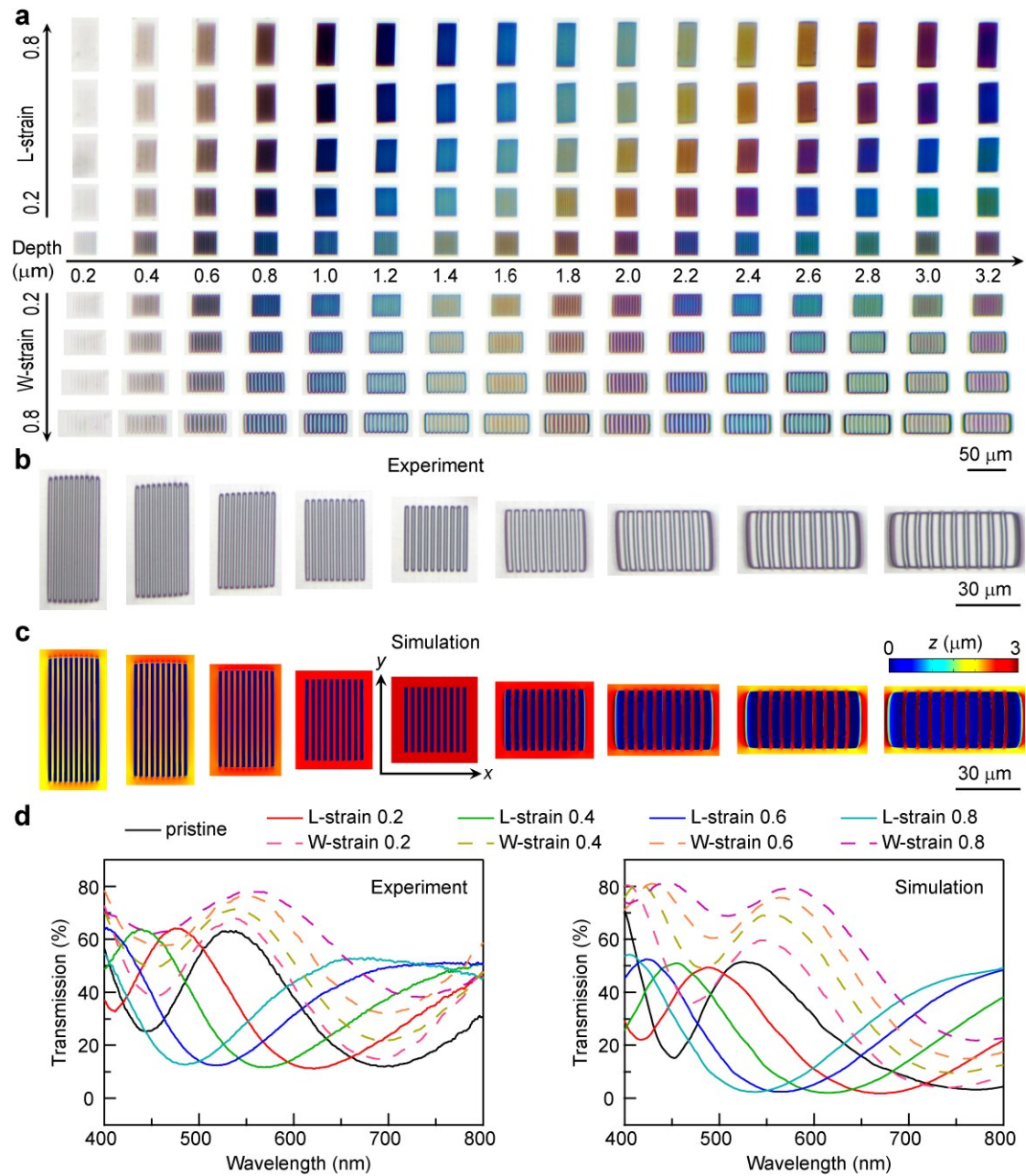


Fig. 2 | Directional strain modulated colours. **a**, Composite transmission optical micrographs of the PDMS trench arrays with depths varying from 0.2 μm to 3.2 μm stretched either along the length or width directions. The pristine PDMS trench arrays have lengths of 30 μm, widths of 1.55 μm, and pitches of 3 μm. The engineering strains are increased from 0 to 0.8 in steps of 0.2. **b**, High-magnified reflection optical images of the directional strain modulated PDMS trenches, captured using a 50× objective. The representative PDMS trenches with an initial depth of 2.8 μm are stretched along their length or width directions with 0.2, 0.4, 0.6, and 0.8 strains. **c**, Top views of the simulated shape

deformations of the PDMS trenches in (b). d, Measured and simulated strain-modulated transmittance spectra of the 2.8- μm -depth PDMS trenches.

Based on the colour palette in Fig. 1c, we developed a colour matching algorithm to design colourful reliefs on the surface of PDMS slabs (Fig. 3a and Supplementary Fig. 8). IP-Dip cuboids with different heights (Fig. 3b) were 3D printed and used as the template to mould colourful pixels on the PDMS slab. Once the PDMS relief is stretched along the length of the trenches, the image of a turtle is elongated with dramatic changes in colour (Fig. 3c). When W-strain is applied, the turtle grows taller with reduced colour saturation (Fig. 3d). The colour switching for the turtle during multiple stretching/releasing cycles were monitored (Supplementary Fig. 9 and 10). Remarkably, the modulation of structural colours in our PDMS reliefs is highly reversible. The directional strain-modulated colours of the turtles during 200 cycles are highly consistent with the colour changes shown in Fig. 3.

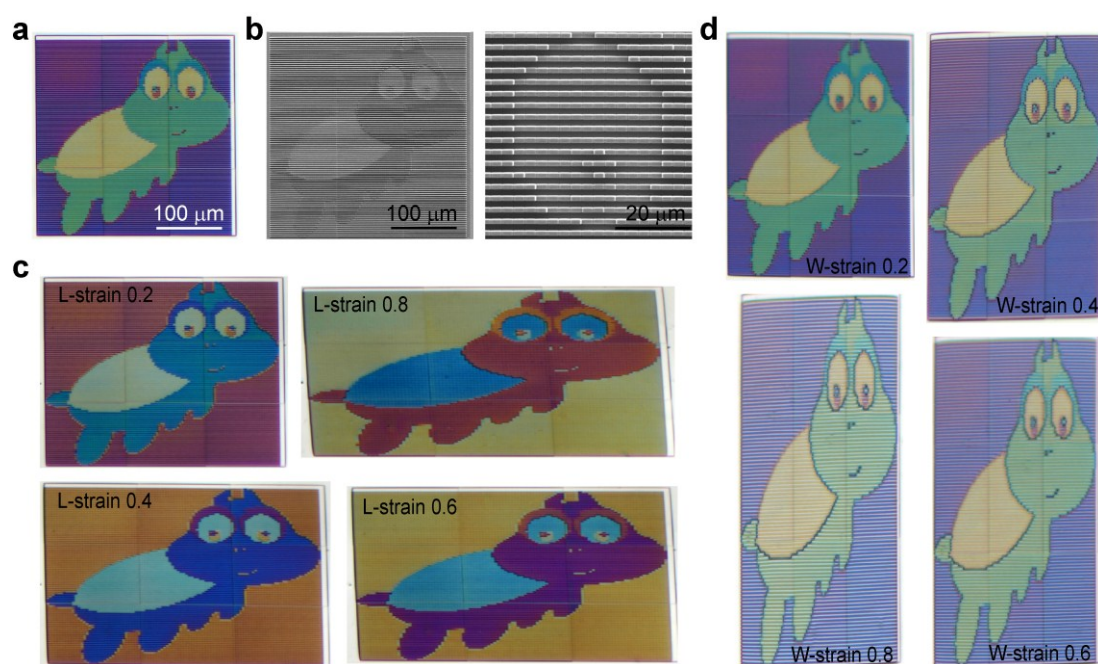


Fig. 3 | Directional strain modulated microprints. a, Transmission optical micrograph of a turtle

made of PDMS trenches with varying depth. **b**, SEM images of the IP-Dip mould used for fabricating the PDMS replica. The area around the eye is enlarged to show the cuboid structures. Each pixel consists of a single cuboid with a length of 3 μm , width of 1.55 μm , and pitch of 3 μm . **c,d**, Optical images of the turtle when 0.2, 0.4, 0.6, and 0.8 strains along the length direction (**c**) and width direction (**d**) of the trenches are employed. All of the optical images share the same scale bar in (**a**).

The shapes and colours of the PDMS trenches can be further affected by capillary forces (Fig. 4a). Methanol was dropped on the surface of the PDMS slabs, and dried under ambient conditions. As methanol evaporates to the level of the trenches, a meniscus is formed between adjacent PDMS ridges, yielding a capillary force. If the balance between the capillary force and elastic restoring force is broken, the neighbouring ridges will merge. Once dried, the collapsed PDMS trenches are kept together by short-range van der Waals' forces between the ridges in contact. PDMS trenches with depths of 1.8 μm or larger were found to collapse and lose their colour. The instabilities in the evaporating process also result in random collapsed patterns without distinct regularity (Supplementary Fig. 11). The effect of elastocapillary coalescence has also been observed in the clumping of wet hair³⁶, as well as the self-assembly of micropillars³⁷ and nanopillars^{38,43}. Pillar arrays with smaller inter-pillar distances and larger heights tend to be collapsed during the evaporation process^{37,38}. As methanol has a high affinity with PDMS surfaces, the critical height H , above which two PDMS cuboids come into contact and collapse, is estimated as⁴⁴

$$H = \sqrt[4]{\frac{EW_{\text{PDMS}}^3W_{\text{air}}^2}{24\gamma}} \quad (3)$$

where E (1.06 MPa, Supplementary Fig. 4) is the Young's modulus of PDMS, γ (22.5 $\text{mN}\cdot\text{m}^{-1}$) is the surface tension of methanol. For the PDMS cuboids with a width of 1.45 μm (W_{PDMS}) and gap distance

of $1.55 \mu\text{m}$ (W_{air}), H is calculated to be $1.95 \mu\text{m}$, which is close to the observed critical trench depth of $1.8 \mu\text{m}$. When stretched along the width direction of the trenches, the elastic restoring force will gradually surpass the van der Waals' forces to separate the touching ridges. After release, the shapes, colours, and transmission spectra of the PDMS trenches fully recovered (Fig. 4a,b, and Supplementary Fig. 11). As methanol possesses a low vapour pressure and barely swells PDMS, it is suitable for rapid evaporation in this study. Solvents with a solubility parameter similar to that of PDMS will extensively swell PDMS, and are expected to alter its mechanical properties^{45,46}. The surface tension of the solvents and the surface chemistry⁴⁷ of the PDMS reliefs should also be considered to elegantly control the capillary force-induced collapse and the adhesion between neighbouring structures.

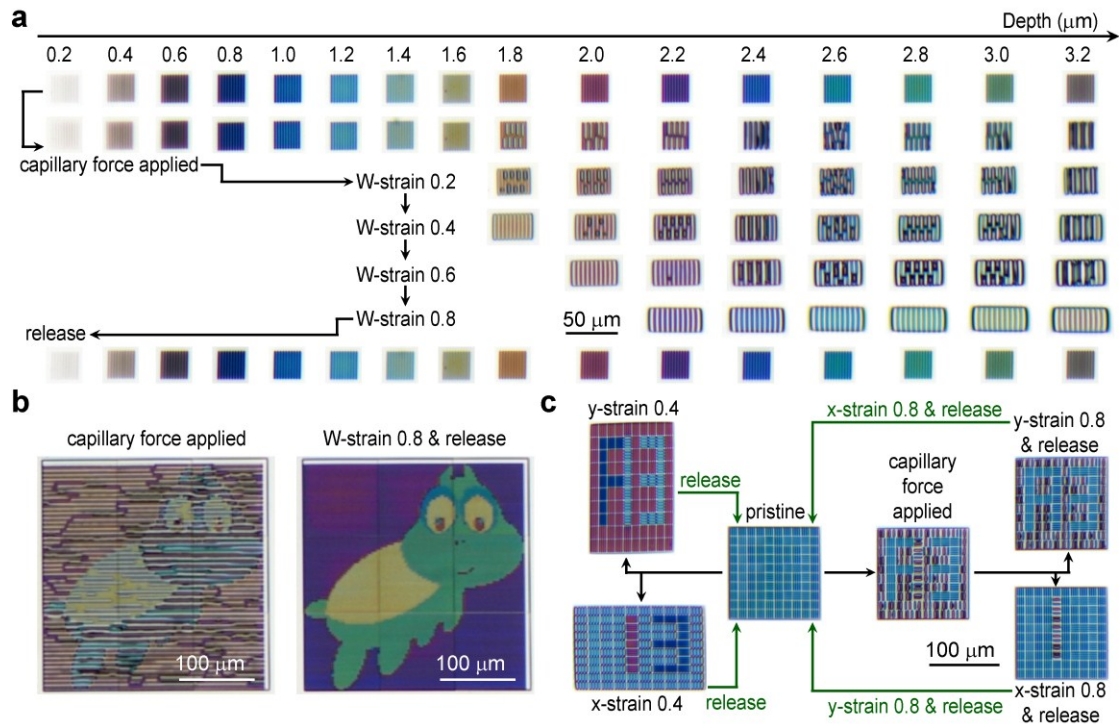


Fig. 4 | Complex states of stretched reliefs incorporating directional recovery of collapsed

trenches. **a**, Transmission optical micrograph of the PDMS trench arrays. When applied with capillary force, trenches with a depth larger than $1.8 \mu\text{m}$ collapse. The collapsed trenches recover in distinct

steps with increasing strain along their width. **b**, Optical images of a turtle scrambled by the capillary force and recovered by a 0.8 strain along the width direction. **c**, Transmission optical images of PDMS trenches encoded with multiple sets of hidden information: the pristine blue pattern displays "F13" or "13", when a strain is employed along the y or x direction, respectively. "F3" is exhibited as surrounding deep trenches collapse by capillary force. "A3" ("1") is decrypted once the collapsed trenches with their length along the x (y) direction get unstuck by applying and removing the y -strain (x -strain), but is hidden again when the residual collapsed trenches are recovered by applying and removing the x -strain (y -strain).

The depth-dependent collapse and directional-strain recovery behaviours of the PDMS trenches, together with the directional strain modulated structural colours, make it possible to design security prints with multiple encrypted information (Fig. 4c). IP-Dip cuboids with heights of 1 and 2.4 μm , and lengths along the x or y directions, were printed at strategic coordinates (Supplementary Fig. 12) and used to replica-mould the PDMS relief. Four types of pixels were produced, which can be named as 1x, 1y, 2.4x, and 2.4y pixels according to the depth values and length directions of the PDMS trenches. As PDMS trenches with depths of 1 and 2.4 μm exhibit similar blue hue (Fig. 1e), the PDMS relief appears as a blank panel with 10×10 blue pixels. When a 0.4 strain is applied along the y direction, 1y pixels turn to dark blue to form a letter "F"; both 2.4x and 1x pixels become light blue to construct a number "13"; 2.4y pixels act as the purple background. Similarly, a purple "1" and a dark blue "3" with a light blue background are observed with a 0.4 x -strain employed. Moreover, the 2.4x and 2.4y pixels can be scrambled by the capillary force, giving rise to a blue "F3" with 1x and 1y pixels. If a 0.8 y -strain is employed and then released, the 2.4x pixels are recovered to a blue vertical line to convert

the letter "F" to "A". In contrast, a 0.8 x-strain can recover the 2.4y pixels, leaving a collapsed grey "1" in a blue background. The pattern will resume to the initial blank panel after all pixels are recovered by the 0.8 x-strain and y-strain. Five sets of covert information have been demonstrated here with strains of only two amplitudes and PDMS trenches of only two depths. More complex information could be encoded based on our approach, if trenches with more choices of depths are produced and multiple amplitudes of directional strains are used.

With the understanding that trenches that are either touching or sufficiently narrow do not generate colour, we proceeded to encode hidden information in transparent PDMS nanotrenches with small widths (Fig. 5). The transparent PDMS nanotrenches with widths of 0.32 μm and pitches of 3 μm are converted into colour pixels when a 0.8 strain is applied along their width direction (Fig. 5a). The emergence of colours is ascribed to the strain-enlarged width of the trenches, as observed both in the experiment (Supplementary Fig. 13) and simulation (Fig. 5b). An image of a fish was then encoded using PDMS nanotrenches with different depths (Fig. 5c, and Supplementary Fig. 14). The transparent PDMS relief reveals a clear fish image upon a 0.8 strain along the width direction of the trenches being placed. The fish is concealed again when the strain is removed. The fish was then repeatedly decrypted and encrypted for 200 cycles (Supplementary Fig. 15). The fish image was highly reproducible in the stretching states, while some residual stress-induced random lines were occasionally observed in the release states.

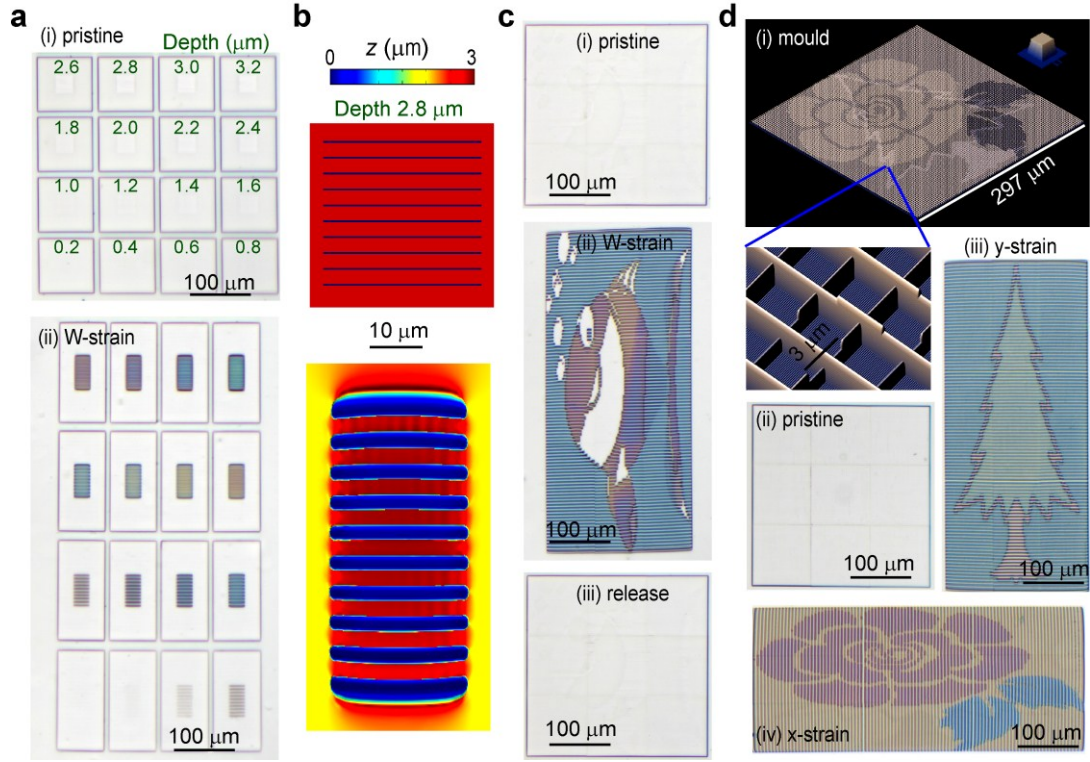


Fig. 5 | Covert images with nanoreliefs revealed by directional strains. **a**, Transmission optical micrographs of narrow PDMS trench arrays at the pristine state (i) and with a 0.8 strain applied along their width direction (ii). The nanotrench arrays have designed lengths of 30 μm, widths of 0.32 μm, pitches of 3 μm, and depths varying from 0.2 to 3.2 μm. **b**, Simulated shape deformation of a representative PDMS nanotrench array with a depth of 2.8 μm. **c**, Optical images of a PDMS relief consists of nanotrenches with programmed depths. The transparent PDMS slab (i, pristine state) discloses a fish when it is stretched along the width direction of the trenches (ii, 0.8 W-strain), and recovers to transparent upon release (iii, release state). **d**, A PDMS relief designed with two covert images. (i) Tilted view of the designed IP-Dip mould in Describe software. Images of a tree and a flower with 99×99 pixels are encoded in the same area. Each pixel contains two orthogonally interlaced cuboids with lengths of 3 μm, widths of 0.32 μm, and varying depths. The transparent area of the PDMS relief (ii) reveals an image of a tree (iii) or a flower (iv) with a 0.8 strain employed along the y or x directions, respectively.

A PDMS relief with two covert images was designed using two orthogonally interlaced nanotrench arrays (Fig. 5d). Images of a tree and a flower are selectively displayed by the strains along the y and x directions, respectively. By applying strain along the y -axis, the x -trenches broaden, while the y -trenches close (Supplementary Fig. 16), thus eliminating potential cross talk between the two sets of images. When the strains are removed, the tree and flower will be hidden again. In addition to the colour shifts (Fig. 3) and the scrambled/recovered colours (Fig. 4) shown in the microprints with microtrenches, the nanoreliefs exhibit covert colourful images from a colourless and featureless initial state.

The IP-Dip cuboids moulds are capable of producing multiple PDMS replicas without noticeable defects (Supplementary Fig. 17). This approach could be extended for replica-moulding surface reliefs in self-healing⁴⁸, electroactive^{49,50}, liquid crystal⁵¹, and other custom-made functional elastomers²⁸. The achievable structural parameters of the reliefs are influenced by the mechanical properties and surface chemistry of the elastomers. Reliefs with arbitrarily oriented trenches possess more intricate shape deformation behaviours. Supplementary Fig. 18 shows the uniaxial strain modulated radial arrays of PDMS trenches. The pristine radial arrays exhibit depth-dependent colours similar to the trench arrays in Fig. 1e. With a uniaxial strain applied, the shape and colour of different parts of the radial arrays undergo more complex changes than observed in co-linear trenches. The shape and colour deformation depends not only on the orientation of the trenches, but also on the presence of neighbour trenches. Each replica-moulded trench discussed in this work is designed with the same cross section along its z -dimension. With the additional design freedom in complex 2.5D and 3D structures^{52,53}, greater complexity in strain-modulated behaviour remains to be explored.

PDMS has been widely used to make flexible moulds in soft lithography^{54,55}. A single PDMS relief sample could in turn be used as a mould for creating multiple distinct replicas when strained appropriately. A variety of Ormostamp replicas were successfully moulded from the same piece of PDMS template (Supplementary Fig. 19). The heights, widths, and pitches of the Ormostamp cuboids can be determined by the strain loaded on the PDMS relief. In addition to the UV-curable transparent Ormostamp resin, the stretchable PDMS reliefs are expected to be used in patterning functional materials, such as hydrogels^{24,56,57}, organogels¹⁸, shape memory polymers^{58,59}, and high-refractive-index resins⁶⁰, with programmed structures.

Conclusion

The basic building block in the form of the trench in the common PDMS elastomer effectively exhibits complex spectral changes that are not diffractive in nature. These monolithic elastomers avoid potential cracking and delamination in systems with multiple materials, thus exhibit highly repeatable and reversible mechanochromic effects. We expect that soft elastomers with 3D reliefs to be employed in further controlling the phase, polarization, and angular momentum of light in the visible spectrum and beyond. While we have only explored stretch-induced strains, compressing the reliefs can also serve as soft templates for moulding functional materials with improved resolution. We believe the flexible reliefs will find applications in steganography, soft lithography, and directional strain sensing.

Methods

3D printing of cuboid array templates. The cuboid structures were printed using a two-photon polymerization lithography system (Photonic Professional GT, Nanoscribe GmbH). A cleaned fused

silica substrate ($25 \times 25 \text{ mm}^2$) was put on a hotplate at 120°C for 10 mins, and cooled to room temperature. In order to increase the adhesion between the substrate and the printed structures, the substrate was spin-coated with TI PRIME adhesion promoter (MicroChemicals GmbH) at 2000 rpm for 20 s, then baked at 120°C for 2 mins. An immerse objective lens (Zeiss Plan Apo 63 \times , NA = 1.4) was used to focus femtosecond laser pulses (780 nm) into the photoresist IP-Dip (Nanoscribe GmbH) using the Dip-in Laser Lithography configuration. An optimal laser power of 20 mW, scan speed of 30 mm/s, hatching distance of 0.1 μm , and slicing distance of 0.2 μm were used. A base layer of 1- μm thickness was added for each writing field in the design to compensate for errors in identifying the interface between the substrate and the resist⁶¹. After patterning, the samples were developed in polyethylene glycol methyl ether acetate (5 mins), isopropyl alcohol (2 mins), and nonafluorobutyl methyl ether (2 mins). The sample was placed on a hotplate at 120°C for 2 mins, cooled to room temperature, then spin-coated with a BGL-GZ-83 (Profactor GmbH) anti-sticking layer at 2000 rpm for 30 s, and used as a template afterwards.

Replica moulding and mechanically controlling PDMS reliefs. PDMS (Dow-Sylgard 184, Dow Corning) with a prepolymer-to-curing agent ratio of 20 : 1 was extensively mixed and degassed in vacuum. The PDMS mixture was poured onto the cuboid array mould, and degassed again to further remove air bubbles. The sample was kept in an oven for 10 h at 70°C to fully cure PDMS and cooled to room temperature. The cured PDMS slab was gently peeled off the mould. Cuboid trenches were therefore formed on the surface of the PDMS slab. A colour matching algorithm was used to convert the colour of each pixel to the structural parameters of the reliefs. Uniaxial strains were applied on the PDMS slab using a custom-built mechanical stretcher. Methanol was dropped on the PDMS relief to cover the trench area. As the methanol evaporated under ambient conditions, some deep trenches were

collapsed by the induced capillary force.

Replica moulding of Ormostamp. Ormostamp (Microresist GmbH) was dropped on the pre-strain PDMS relief and then covered by a glass slide. The resist was cured using UV light (BlueWave MX-150, Dymax) for 30 seconds with 40% maximum power, and peeled off from the PDMS mould. Ormostamp slabs with different patterns were obtained when different strains were applied on the same piece of flexible PDMS mould.

Optical measurements. The optical micrographs and transmittance spectra were taken by a Nikon Eclipse LV100ND optical microscope equipped with a Nikon DS-Ri2 camera and a CRAIC 508 PV microspectrophotometer. Two halogen lamps (LV-HL 50 W) were used to illuminate the samples in the reflection/transmission mode. A 5 \times , NA = 0.15 objective was employed to measure the transmission images and transmission spectra. The spectra were normalized to the transmittance spectrum of the non-patterned area of the PDMS slabs. A 50 \times , 0.4 NA objective was used to capture the high-magnified images of the PDMS trenches in the reflection mode.

Characterization. The SEM images were recorded with a JSM-7600F Schottky Field Emission Scanning Electron Microscope (JEOL, Japan) using a voltage of 5 kV. The samples were sputtered with Pt/Pd for 30 seconds with a current of 40 mA at the control gas manual mode before SEM imaging. The uniaxial tensile experiment on the PDMS slab was conducted on a dynamic mechanical analyzer (Q800 DMA, TA Instruments).

Simulation. The strain-induced shape deformation of the PDMS trenches was carried out using a finite element method based software (COMSOL Multiphysics). The experimental tensile test data of the PDMS slab was fitted by a two-parameter incompressible Mooney-Rivlin model and imported into COMSOL. To apply directional strain on the PDMS slab, the fixed constraint was set at one boundary

and the prescribed displacement condition was employed at the opposite boundary. The strain-induced shape deformation and von Mises stress plot were obtained. The transmission and scattering spectra of the PDMS trenches were conducted with a finite-difference time-domain software (Lumerical Solution). PDMS was modelled with the experimentally measured dispersive refractive index⁶². The directional strains modulated shapes of the PDMS trenches were obtained from the COMSOL simulation. For the transmission spectra, a plane wave was normally incident the PDMS trenches with periodic boundary conditions. A field and power monitor was placed above the PDMS trenches and a near-to-far-field projection was performed to integrate the transmitted light within an 8.6° cone, which corresponds to the numerical aperture of the experimentally used $5\times$ objective lens. The calculated spectra were normalized to a reference transmission spectrum of a flat PDMS slab without the air trenches. For the scattering spectra of the single PDMS trench, a total-field scattered-field source and perfectly matched layer absorbing boundary conditions were used. Two field and power monitors were placed outside the source area to obtain the forward and backward scattering spectra, respectively.

Data availability

All data are available from the corresponding author upon reasonable request.

Acknowledgements

This research is supported by National Research Foundation (NRF) Singapore, under its Competitive Research Programme NRF-CRP001-021 and CRP20-2017-0004. We sincerely thank Soroosh Daqiqeh Rezaei, Antónia Monteiro, Cédric Finet, and Bei Yi Yang for their useful discussion.

Author Contributions

Q.F.R. conceived the idea, performed the design, fabrication, measurement and simulation. W.Z. assisted in the uniaxial tensile experiment and COMSOL simulation. H.W. and H.T.W. drew the schematic diagrams. J.Y.E.C., H.W. and H.L.L. assisted in developing the algorithm for generating 3D printing files. D.Y.F., Y.L., C.-W.Q., and J.K.W.Y. supervised the research. All the authors discussed the results and contributed to the manuscript.

Conflict of Interest

The authors declare no conflict of interest.

References

- 1 Gu, B. *From Oracle Bones to Computers: the Emergence of Writing Technologies in China* (Parlor Press LLC, 2009).
- 2 Robinson, A. Thomas Young and the Rosetta Stone. *Endeavour* **31**, 59–64 (2007).
- 3 Cooper, G. *The Origin of Financial Crises* (Vintage, New York, 2008).
- 4 Pohlmann, K. C. *The Compact Disc Handbook* (Oxford Univ. Press, 1992).
- 5 Kats, M. A., Blanchard, R., Genevet, P., & Capasso, F. Nanometre optical coatings based on strong interference effects in highly absorbing media. *Nat. Mater.* **12**, 20–24 (2013).
- 6 Wang, Z. *et al.* Towards full-colour tunability of inorganic electrochromic devices using ultracompact fabry-perot nanocavities. *Nat. Commun.* **11**, 302 (2020).
- 7 Goodling, A. E. *et al.* Colouration by total internal reflection and interference at microscale concave interfaces. *Nature* **566**, 523–527 (2019).
- 8 Wu, P. P., Wang, J. X., & Jiang, L. Bio-inspired photonic crystal patterns. *Mater. Horiz.* **7**, 338–365 (2020).
- 9 Neubrech, F., Duan, X., & Liu, N. Dynamic plasmonic color generation enabled by functional materials. *Sci. Adv.* **6**, eabc2709 (2020).
- 10 Shao, L., Zhuo, X. L., & Wang, J. F. Advanced plasmonic materials for dynamic color display. *Adv. Mater.* **30**, 1704338 (2018).
- 11 Dong, Z. G. *et al.* Printing beyond sRGB color gamut by mimicking silicon nanostructures in free-space. *Nano Lett.* **17**, 7620–7628 (2017).
- 12 Yang, W. H. *et al.* All-dielectric metasurface for high-performance structural color. *Nat. Commun.* **11**, 1864 (2020).
- 13 Kristensen, A. *et al.* Plasmonic colour generation. *Nat. Rev. Mater.* **2**, 16088 (2016).

- 14 Kumar, K. *et al.* Printing colour at the optical diffraction limit. *Nat. Nanotechnol.* **7**, 557–561 (2012).
- 15 Zhu, X. L. *et al.* Plasmonic colour laser printing. *Nat. Nanotechnol.* **11**, 325–329 (2016).
- 16 Daqiqeh Rezaei, S. *et al.* Nanophotonic structural colors. *ACS Photonics* **8**, 18–33 (2020).
- 17 Duan, X. Y., Kamin, S., & Liu, N. Dynamic plasmonic colour display. *Nat. Commun.* **8**, 14606 (2017).
- 18 Oh, J. *et al.* Dynamic multimodal holograms of conjugated organogels via dithering mask lithography. *Nat. Mater.* **20**, 385–394 (2021).
- 19 Lopez-Garcia M. *et al.* Light-induced dynamic structural color by intracellular 3D photonic crystals in brown algae. *Sci. Adv.* **4**, eaan8917 (2018).
- 20 Matsubara, K., Watanabe, M., & Takeoka, Y. A thermally adjustable multicolor photochromic hydrogel. *Angew. Chem., Int. Ed.* **46**, 1688–1692 (2007).
- 21 Huang, M. T. *et al.* Voltage-gated optics and plasmonics enabled by solid-state proton pumping. *Nat. Commun.* **10**, 5030 (2019).
- 22 Yan, Z. Y. *et al.* Floating solid-state thin films with dynamic structural colour. *Nat. Nanotechnol.* **16**, 795–801 (2021).
- 23 Kim, H. *et al.* Structural colour printing using a magnetically tunable and lithographically fixable photonic crystal. *Nat. Photon.* **3**, 534–540 (2009).
- 24 Zhang, Y. L. *et al.* Super-elastic magnetic structural color hydrogels. *Small* **15**, 1902198 (2019).
- 25 Castles, F. *et al.* Stretchable liquid-crystal blue-phase gels. *Nat. Mater.* **13**, 817–821 (2014).
- 26 Kose, O. *et al.* Unwinding a spiral of cellulose nanocrystals for stimuli-responsive stretchable optics. *Nat. Commun.* **10**, 510 (2019).
- 27 Qin, D., Xia, Y. N., & Whitesides, G. M. Soft lithography for micro-and nanoscale patterning. *Nat. Protoc.* **5**, 491–502 (2010).
- 28 Mazurek, P., Vudayagiri, S., & Skov, A. L. How to tailor flexible silicone elastomers with mechanical integrity: a tutorial review. *Chem. Soc. Rev.* **48**, 1448–1464 (2019).
- 29 Qi, D. P., Zhang, K. Y., Tian, G. W., Jiang, B., & Huang, Y. D. Stretchable electronics based on PDMS substrates. *Adv. Mater.* **33**, 2003155 (2020).
- 30 Tseng, M. L. *et al.* Two-dimensional active tuning of an aluminum plasmonic array for full-spectrum response. *Nano Lett.* **17**, 6034–6039 (2017).
- 31 Zhang, C. *et al.* Stretchable all-dielectric metasurfaces with polarization-insensitive and full-spectrum response. *ACS Nano* **14**, 1418–1426 (2019).
- 32 Lee, G. H. *et al.* Chameleon-inspired mechanochromic photonic films composed of non-close-packed colloidal arrays. *ACS Nano* **11**, 11350–11357 (2017).
- 33 Zhou, Q. T. *et al.* Multimodal and covert-overt convertible structural coloration transformed by mechanical stress. *Adv. Mater.* **32**, 2001467 (2020).
- 34 Quan, Y.-J., Kim, Y.-G., Kim, M.-S., Min, S.-H., & Ahn, S.-H. Stretchable biaxial and shear strain sensors using diffractive structural colors. *ACS Nano* **14**, 5392–5399 (2020).
- 35 Zhao, P. F. *et al.* Stretchable photonic crystals with periodic cylinder shaped air holes for improving mechanochromic performance. *Smart Mater. Struct.* **28**, 075037 (2019).
- 36 Bico, J., Roman, B., Moulin, L., & Boudaoud, A. Elastocapillary coalescence in wet hair. *Nature* **432**, 690–690 (2004).
- 37 Hu, Y. *et al.* Laser printing hierarchical structures with the aid of controlled capillary-driven self-assembly. *Proc. Natl. Acad. Sci. U. S. A.* **112**, 6876–6881 (2015).

- 38 Pokroy, B., Kang, S. H., Mahadevan, L., & Aizenberg, J. Self-organization of a mesoscale bristle into ordered, hierarchical helical assemblies. *Science* **323**, 237–240 (2009).
- 39 Knop, K. Rigorous diffraction theory for transmission phase gratings with deep rectangular grooves. *J. Opt. Soc. Am.* **68**, 1206–1210 (1978).
- 40 Grzybowski, B. A., Qin, D., & Whitesides, G. M. Beam redirection and frequency filtering with transparent elastomeric diffractive elements. *Appl. Opt.* **38**, 2997–3002 (1999).
- 41 Gent, A. N. *Engineering with Rubber: How to Design Rubber Components* (Carl Hanser Verlag GmbH Co KG, 2012).
- 42 Park, J. S., Cabosky, R., Ye, Z., & Kim, I. I. Investigating the mechanical and optical properties of thin PDMS film by flat-punched indentation. *Opt. Mater.* **85**, 153–161 (2018).
- 43 Lao, Z. X. *et al.* Mechanical-tunable capillary-force-driven self-assembled hierarchical structures on soft substrate. *ACS Nano* **12**, 10142–10150 (2018).
- 44 Tanaka, T., Morigami, M., & Atoda, N. Mechanism of resist pattern collapse. *J. Electrochem. Soc.* **140**, 6059–6064 (1993).
- 45 Lee, J. N., Park, C., & Whitesides, G. M. Solvent compatibility of poly (dimethylsiloxane)-based microfluidic devices. *Anal. Chem.* **75**, 6544–6554 (2003).
- 46 Li, S. C. *et al.* Liquid-induced topological transformations of cellular microstructures. *Nature* **592**, 386–391 (2021).
- 47 Matsunaga, M., Aizenberg, M., & Aizenberg, J. Controlling the stability and reversibility of micropillar assembly by surface chemistry. *J. Am. Chem. Soc.* **133**, 5545–5553 (2011).
- 48 Guo, H. S., Han, Y., Zhao, W. Q., Yang, J., & Zhang, L. Universally autonomous self-healing elastomer with high stretchability. *Nat. Commun.* **11**, 2037 (2020).
- 49 Peltine, R., Kornbluh, R., Pei, Q., & Joseph, J. High-speed electrically actuated elastomers with strain greater than 100%. *Science* **287**, 836–839 (2000).
- 50 She, A., Zhang, S. Y., Shian, S., Clarke, D. R., & Capasso, F. Adaptive metalenses with simultaneous electrical control of focal length, astigmatism, and shift. *Sci. Adv.* **4**, eaap9957 (2018).
- 51 Kizhakidathazhath, R. *et al.* Facile anisotropic deswelling method for realizing large-area cholesteric liquid crystal elastomers with uniform structural color and broad-range mechanochromic response. *Adv. Func. Mater.* **30**, 1909537 (2020).
- 52 LaFratta, C. N., Li, L., & Fourkas, J. T. Soft-lithographic replication of 3D microstructures with closed loops. *Proc. Natl. Acad. Sci. U. S. A.* **103**, 8589–8594 (2006).
- 53 Chan, H. N. *et al.* Direct, one-step molding of 3D-printed structures for convenient fabrication of truly 3D PDMS microfluidic chips. *Microfluid. Nanofluid.* **19**, 9–18 (2015).
- 54 Pokroy, B., Epstein, A. K., Persson-Gulda, M. C. M., & Aizenberg, J. Fabrication of bioinspired actuated nanostructures with arbitrary geometry and stiffness. *Adv. Mater.* **21**, 463–469 (2009).
- 55 Liu, L., Zhang, J., Badshah, M. A., Dong, L., Li, J., Kim, S. M., & Lu, M. A programmable nanoreplica molding for the fabrication of nanophotonic devices. *Sci. Rep.* **6**, 22445 (2016).
- 56 Liu, C. *et al.* Tough hydrogels with rapid self-reinforcement. *Science* **372**, 1078–1081 (2021).
- 57 Ge, Q. *et al.* 3D printing of highly stretchable hydrogel with diverse UV curable polymers. *Sci. Adv.* **7**, eaba4261 (2021).
- 58 Fang, Y. *et al.* Reconfigurable photonic crystals enabled by pressure-responsive shape-memory polymers. *Nat. Commun.* **6**, 7416 (2015).
- 59 Zhang, W. *et al.* Structural multi-colour invisible inks with submicron 4D printing of shape

- memory polymers. *Nat. Commun.* **12**, 112 (2021).
- 60 Yoon, G., Kim, K., Huh, D., Lee, H., & Rho, J. Single-step manufacturing of hierarchical dielectric metalens in the visible. *Nat. Commun.* **11**, 2268 (2020).
- 61 Wang, H., Wang, H. T., Zhang, W. & Yang, J. K. Toward near-perfect diffractive optical elements via nanoscale 3D printing. *ACS Nano* **14**, 10452–10461 (2020).
- 62 Zhang, X., Qiu, J., Li, X., Zhao, J. & Liu, L. Complex refractive indices measurements of polymers in visible and near-infrared bands. *Appl. Opt.* **59**, 2337–2344 (2020).

Supplementary Information

Reconfiguring colours of single relief structures by directional stretching

Qifeng Ruan,^{1,2} Wang Zhang,² Hao Wang,² John You En Chan,² Hongtao Wang,^{2,3} Hailong Liu,⁴

Dianyuan Fan,¹ Ying Li,^{1,*} Cheng-Wei Qiu,^{3,*} Joel K.W. Yang^{2,4,*}

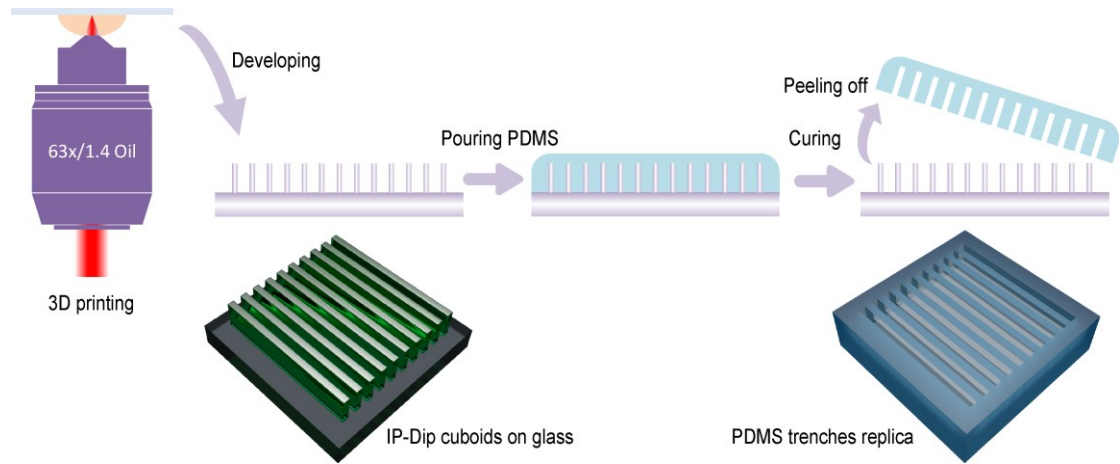
¹*SZU-NUS Collaborative Innovation Center for Optoelectronic Science & Technology, International Collaborative Laboratory of 2D Materials for Optoelectronics Science and Technology of Ministry of Education, Institute of Microscale Optoelectronics, Shenzhen University, Shenzhen 518060, China*

²*Engineering Product Development Pillar, Singapore University of Technology and Design, 8 Somapah Road, Singapore 487372, Singapore*

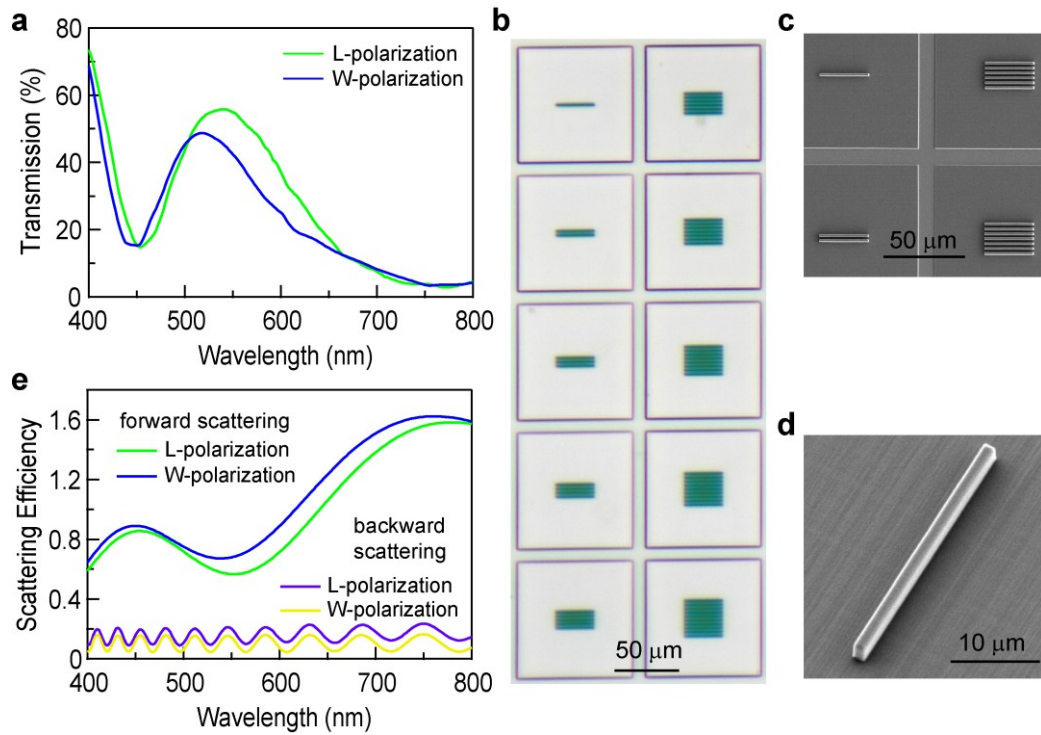
³*Singapore Department of Electrical and Computer Engineering, National University of Singapore, Singapore 117583, Singapore*

⁴*Institute of Materials Research and Engineering, A*STAR (Agency for Science, Technology and Research), Singapore 138634, Singapore*

*queenly@szu.edu.cn; chengwei.qiu@nus.edu.sg; joel_yang@sutd.edu.sg

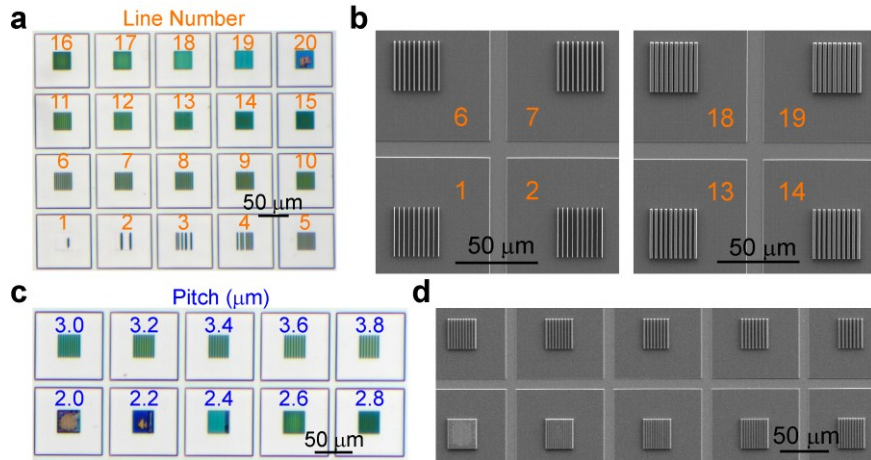


Supplementary Fig. 1 | Schematic of the 3D printing and replica-moulding process to produce polydimethylsiloxane (PDMS) trenches. IP-Dip cuboids are 3D printed in a two-photon polymerization lithography system. After developing, the IP-Dip cuboids on glass substrate are used as the template. Mixed PDMS prepolymer and curing agent is poured onto the template. After curing, PDMS trenches are peeled off from the template.



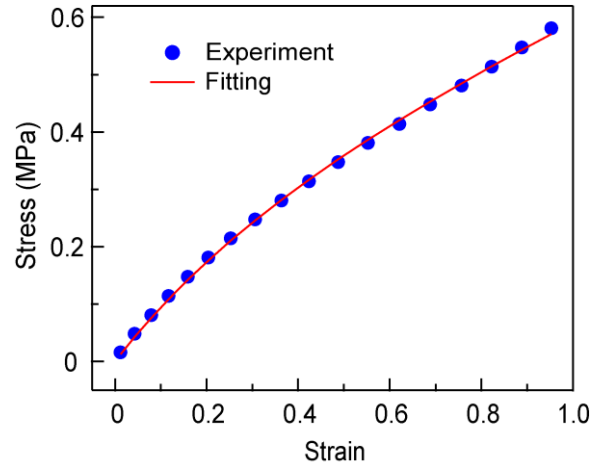
Supplementary Fig. 2 | **a**, Simulated transmission spectra of a PDMS trench array with linear polarized incident light along the length (L-polarization) and width (W-polarization) directions. The

trench arrays have a length of 30 μm , width of 1.55 μm , depth of 2.8 μm , and pitch of 3 μm . **b**, Transmission optical micrograph of PDMS trench arrays with 1 to 10 trenches. **c**, Scanning electron micrograph (SEM) image of the IP-Dip cuboid mould. **d**, 30° tilted view SEM image of a single IP-Dip cuboid. **e**, Simulated forward and backward scattering spectra of a single PDMS trench. Light with a deviation angle smaller than 8.6° can still be collected by the 5 \times , NA = 0.15 objective. To match the experimental setup, only light with a deviation angle in the range of $8.6^\circ - 90^\circ$ is calculated into forward scattering. Light with deviation angle in the range of $90^\circ - 180^\circ$ is counted for backward scattering. The calculated scattering cross sections are divided by the physical cross section of the trench to obtain the scattering efficiencies.



Supplementary Fig. 3 | a, Transmission optical micrograph of PDMS trench arrays with different designed widths but a fixed length of 30 μm , depth of 2.8 μm , and pitch of 3 μm . **b**, SEM images of some representative IP-Dip cuboid moulds for making the PDMS sample in (a). IP-Dip cuboids are printed with different numbers of lines with a hatching distance of 0.1 μm , resulting in cuboid widths in the range of 0.32 – 2.18 μm for line numbers from 1 to 20. **c**, Transmission optical micrograph of

PDMS trench arrays with different designed pitches but a fixed width of 1.55 μm , length of 30 μm , and depth of 2.8 μm . **d**, SEM image of the IP-Dip cuboid moulds for fabricating the PDMS sample in **(c)**.

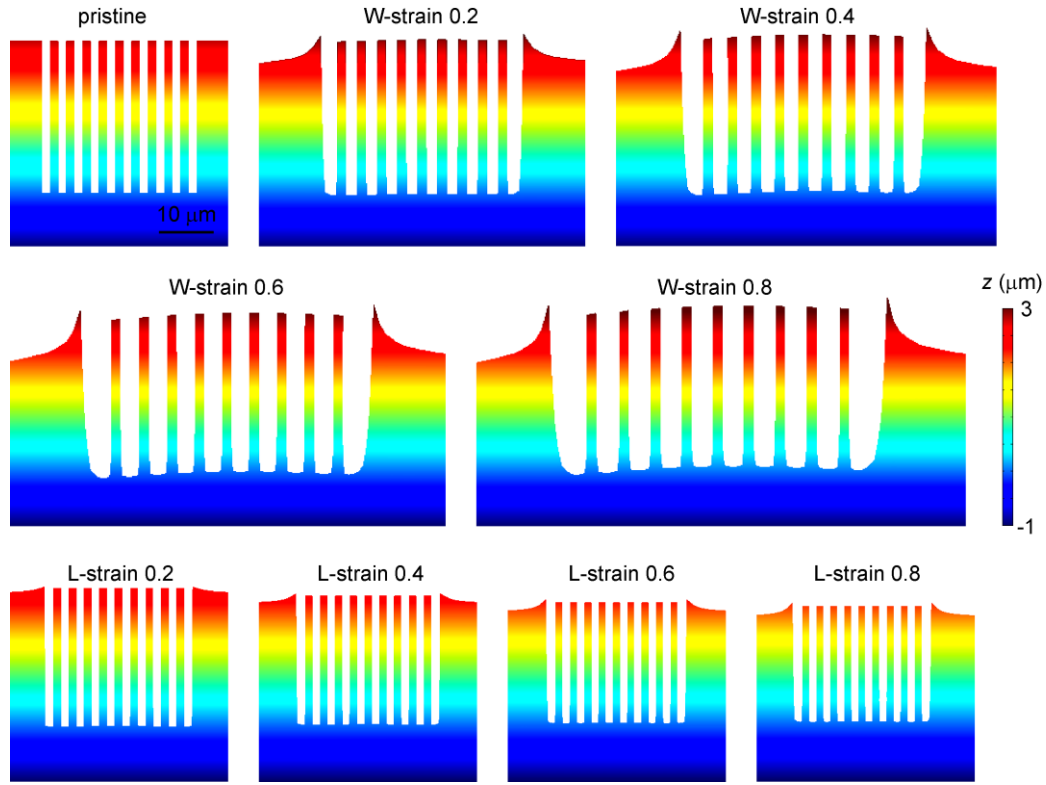


Supplementary Fig. 4 | Strain-stress relationship measured in a uniaxial tensile test on the PDMS slab.

Young's modulus, defined as the initial slope of the stress-strain curve, is calculated to be 1.06 MPa. A two-parameter incompressible Mooney-Rivlin model is used to fit the experimental tensile data of the PDMS material. The Mooney-Rivlin model can be expressed as

$$\sigma = 2 \left(C_{10} + C_{01} \frac{1}{1 + \varepsilon} \right) \left(1 + \varepsilon - \left(\frac{1}{1 + \varepsilon} \right)^2 \right)$$

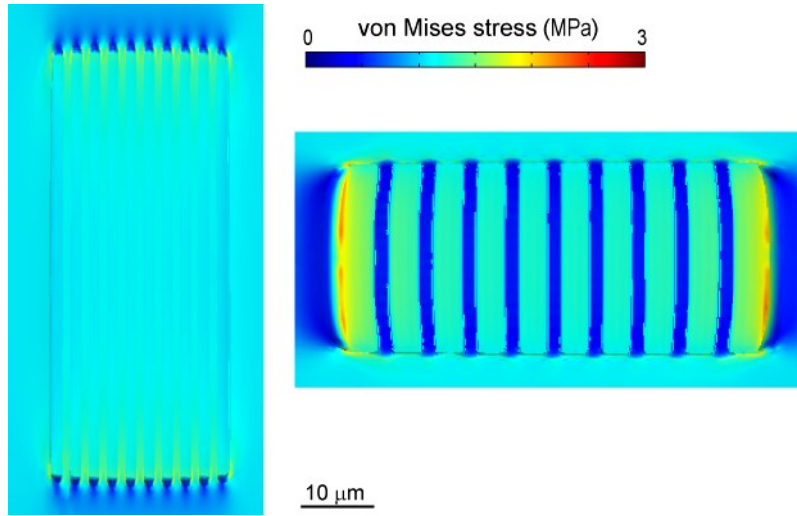
Where σ is stress, ε is engineering strain, C_{10} and C_{01} are material parameters. By fitting the tensile test data, we obtain $C_{10} = 0.1647$ MPa and $C_{01} = 0.0080$ MPa with a coefficient of determination R^2 of 0.9993. The fitted model is input to COMSOL Multiphysics to simulate the deformed configurations.



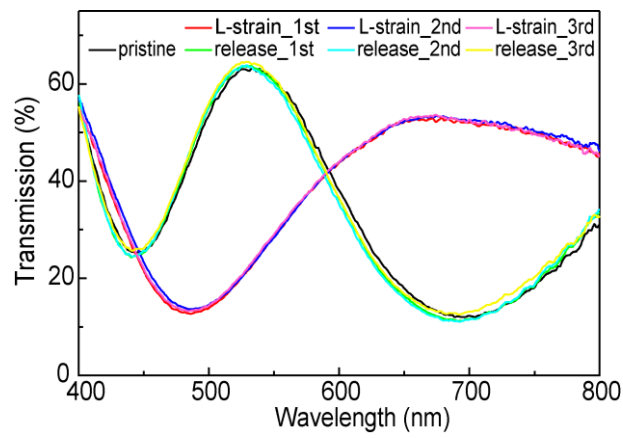
Supplementary Fig. 5 | Cross-sectional views of the simulated shape deformations of the PDMS trenches. The pristine PDMS trench arrays have lengths of 30 μm , widths of 1.55 μm , depths of 2.8 μm , and pitches of 3 μm . The engineering strains along the length or width directions are increased from 0 to 0.8 at a step of 0.2. The xz -cross-sections at the centre of the PDMS trench arrays in Fig. 2c are shown.

Supplementary Table 1 | Simulated shape deformations. The pitch, depth, top width (W_{top}), and bottom width (W_{bottom}) of the trench are measured at the centre of each PDMS trench array.

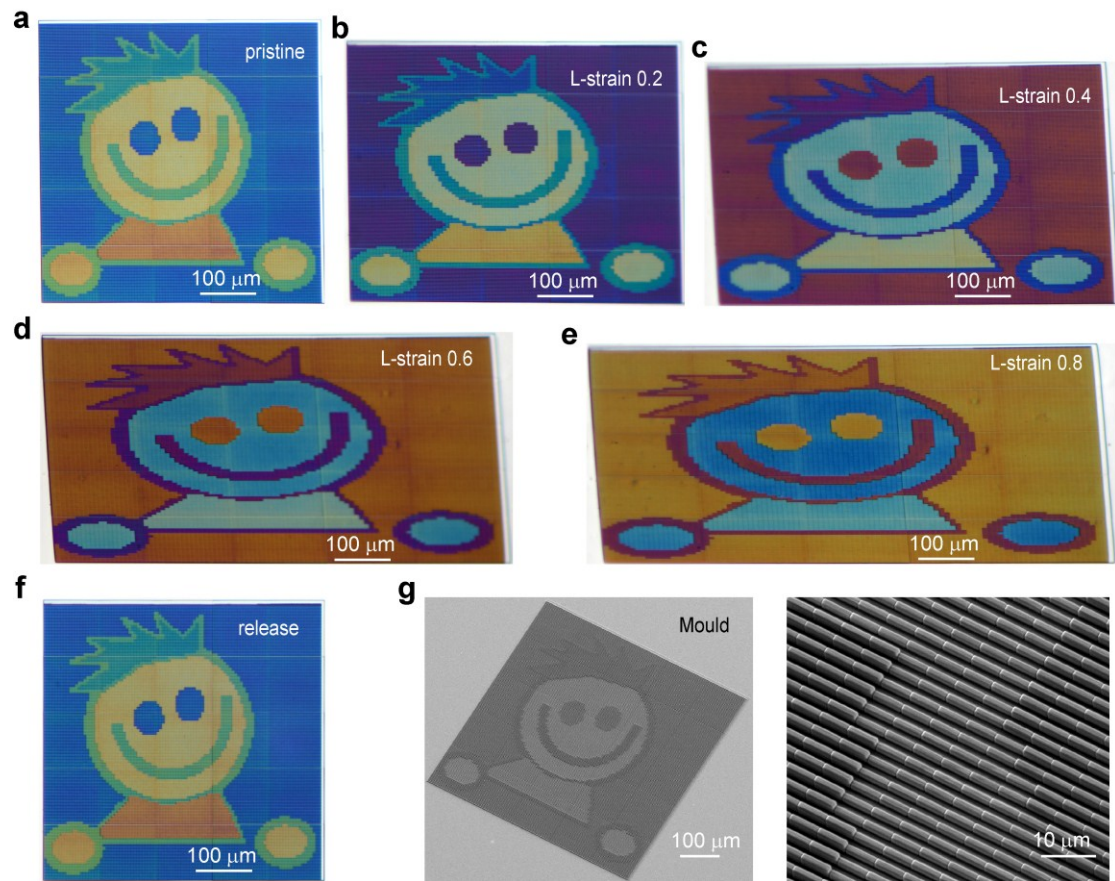
Strain	Pitch (μm)	Depth (μm)	W_{top} (μm)	W_{bottom} (μm)
0	3.00	2.80	1.55	1.55
L-strain 0.2	2.80	2.51	1.49	1.45
L-strain 0.4	2.66	2.31	1.46	1.39
L-strain 0.6	2.54	2.14	1.43	1.33
L-strain 0.8	2.39	1.92	1.38	1.25
W-strain 0.2	3.71	2.85	2.22	1.99
W-strain 0.4	4.35	2.89	2.83	2.43
W-strain 0.6	5.05	2.93	3.50	2.92
W-strain 0.8	5.73	2.97	4.16	3.42



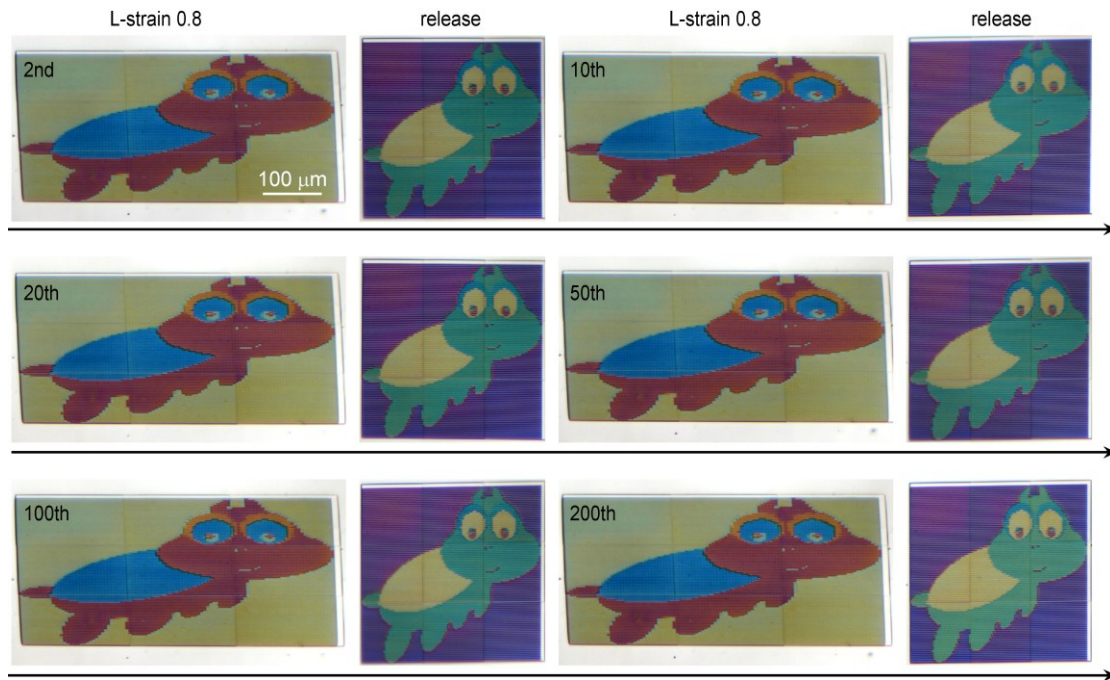
Supplementary Fig. 6 | Simulated von Mises stress distributions of the PDMS trenches with a 0.8 strain loaded along the length or width direction of the trenches.



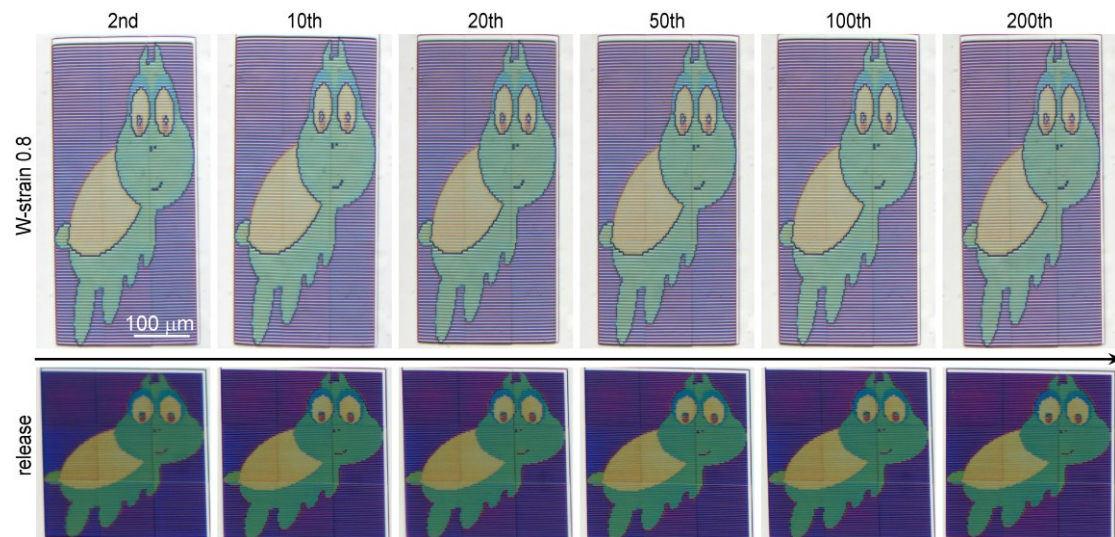
Supplementary Fig. 7 | Measured transmittance spectra of a representative PDMS trench array for 3 stretching/releasing cycles. The pristine PDMS trench array has a length of 30 μm , width of 1.55 μm , depth of 2.8 μm , and pitch of 3 μm . For each cycle, the PDMS slab is stretched with a 0.8 strain along the length direction of the trenches and then released.



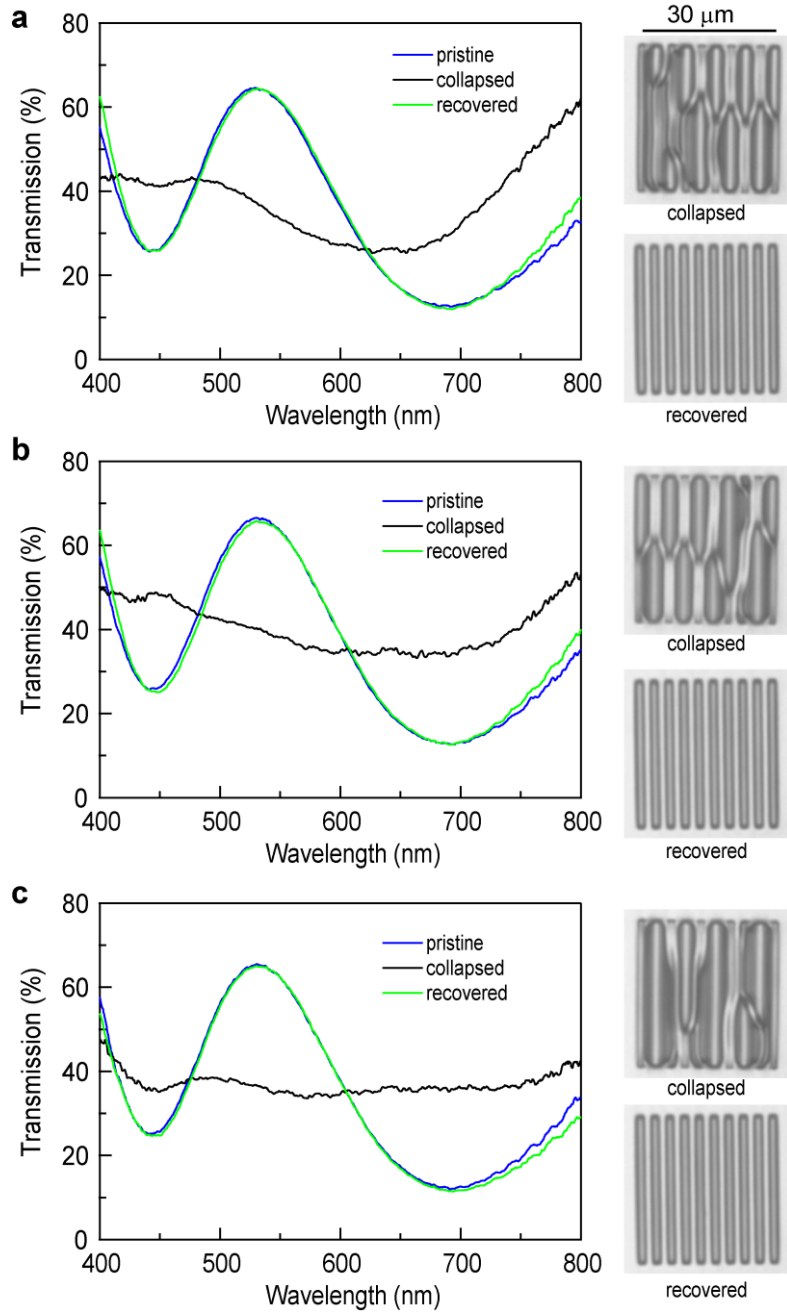
Supplementary Fig. 8 | Another example of directional strain modulated microprints. **a**, Transmission optical micrograph of a boy made of PDMS trenches with varying depths. Each pixel contains two PDMS trenches with a length of 6 µm, width of 1.55 µm, and pitch of 3 µm. **b-f**, Optical images of the boy when the PDMS slab is stretched along the length direction of the trenches with 0.2 (**b**), 0.4 (**c**), 0.6 (**d**), and 0.8 (**e**) strains, and then released (**f**). **g**, 30° tilted view SEM images of the IP-Dip mould used for making the PDMS replica.



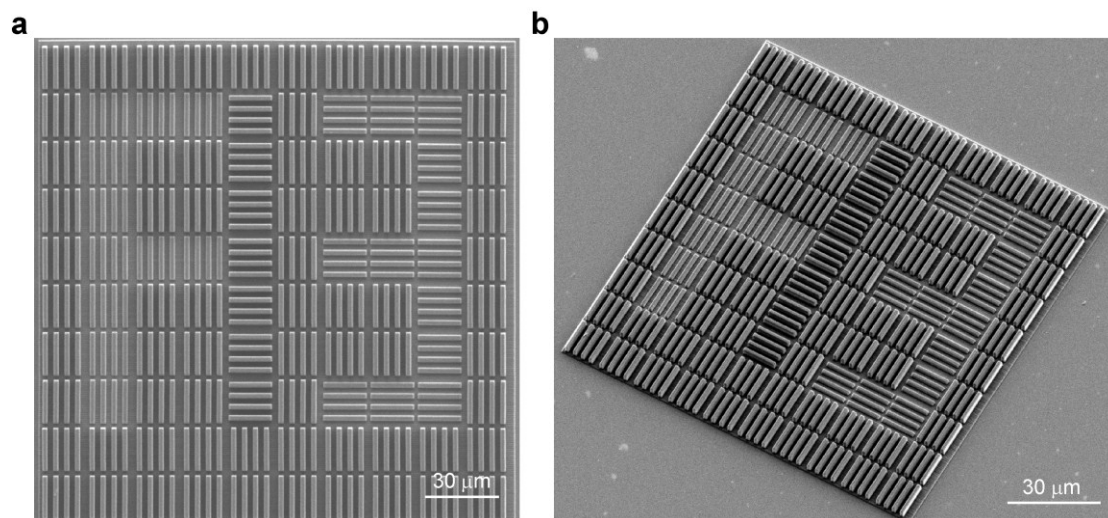
Supplementary Fig. 9 | Transmission optical micrographs of a turtle during 200 L-stretching/releasing cycles. 0.8 strains along the length direction of the trenches are employed and then released for each cycle. All of the images share the same scale bar.



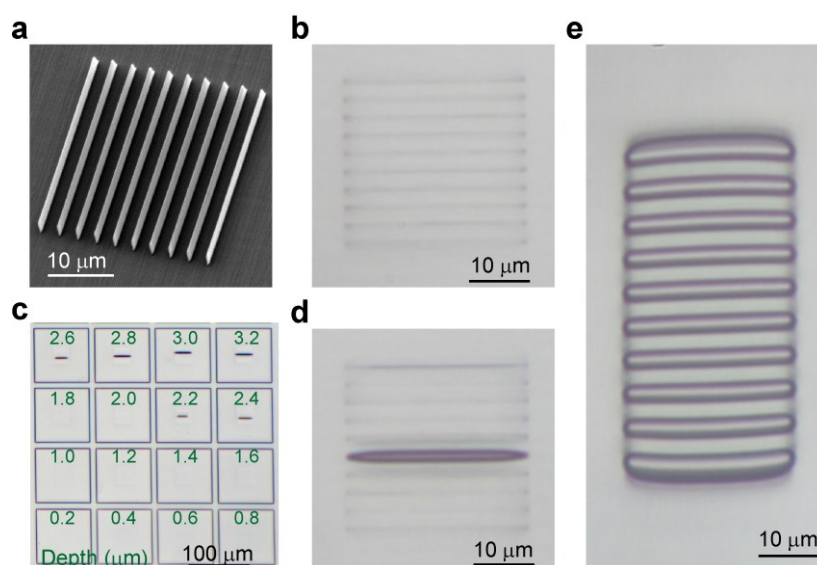
Supplementary Fig. 10 | Transmission optical micrographs of a turtle during 200 W-stretching/releasing cycles. 0.8 strains along the width direction of the trenches are employed and then released for each cycle. All of the images share the same scale bar.



Supplementary Fig. 11 | a-c, Measured transmittance spectra of three representative PDMS trench arrays. The pristine PDMS trench arrays have the same lengths of 30 μm , widths of 1.55 μm , depths of 2.8 μm , and pitches of 3 μm . The trenches are collapsed by the capillary force, and recovered when a 0.8 strain along the width direction of the trenches is applied and released. The high-magnified reflection images of the collapsed and recovered PDMS trenches are shown on the right.

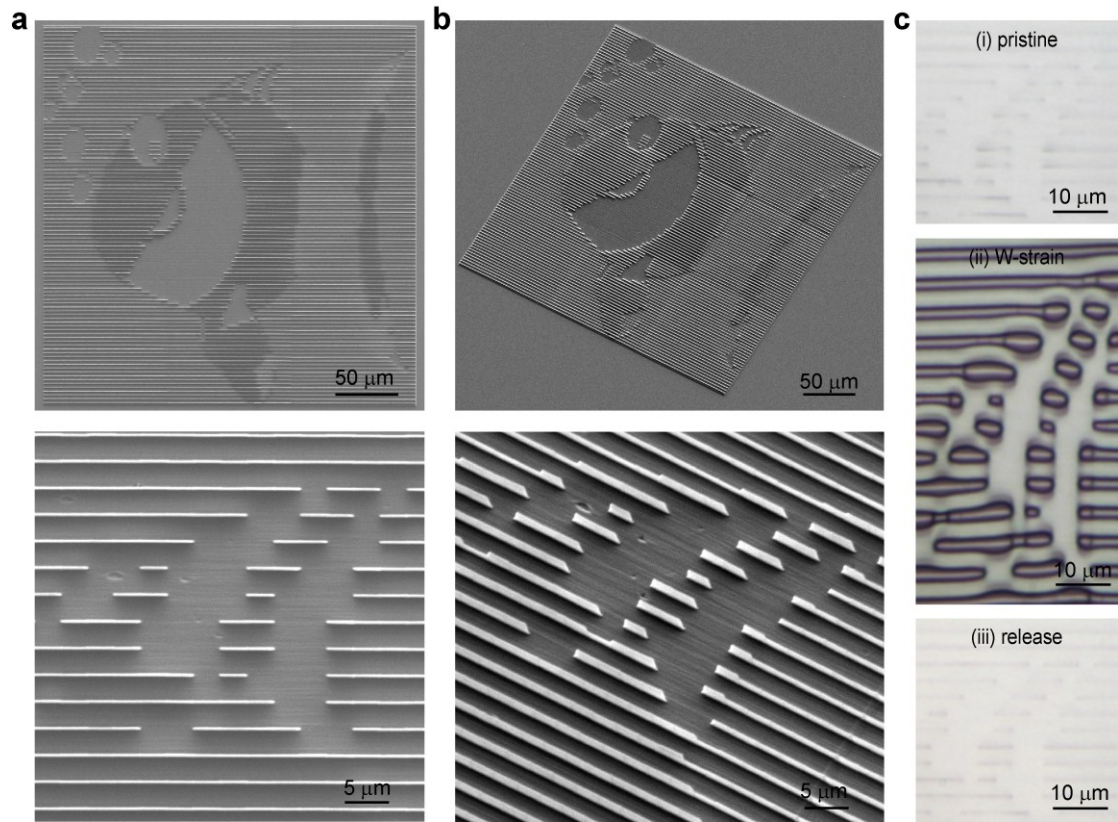


Supplementary Fig. 12 | SEM images of the IP-Dip mould for making the secret print. Top view (a) and 30° tilted view (b) SEM images of the IP-Dip mould used for making the PDMS replica in Fig. 4c. Each pixel contains four cuboids with the same lengths of 12 μm , widths of 1.55 μm , and pitches of 3 μm . A 1- μm gap is placed between the adjacent pixels. The cuboids have a height of either 1 μm or 2.4 μm with the length along either x or y direction.



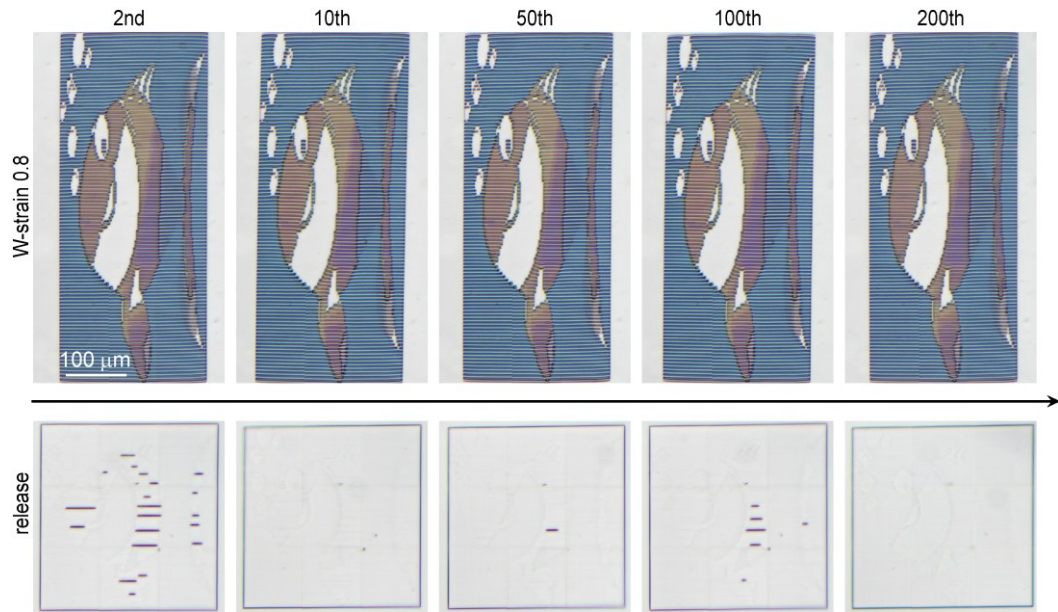
Supplementary Fig. 13 | a, Representative 30° tilted SEM image of an IP-Dip cuboid array with a length of 30 μm , width of 0.32 μm , height of 2.8 μm , and pitch of 3 μm . b, High-magnified reflection

image of a PDMS nanotrench array moulded from the IP-Dip cuboids in (a). c, Transmission optical micrograph of PDMS trench arrays with designed lengths of 30 μm , widths of 0.32 μm , pitches of 3 μm , and depths varying from 0.2 to 3.2 μm . The PDMS trenches in (c) and Fig. 5a are replicas moulded from the same IP-Dip cuboid template. The trenches with depths larger than 2.0 μm are unstable, sometimes exhibiting dark lines. The dark lines are supposed to come from the deformed PDMS trenches, as shown in the reflection image of a representative PDMS trench array with a designed depth of 2.8 μm (d). Both of the PDMS trenches in (b) and (d) can be opened up by a 0.8 strain along their width direction (e).

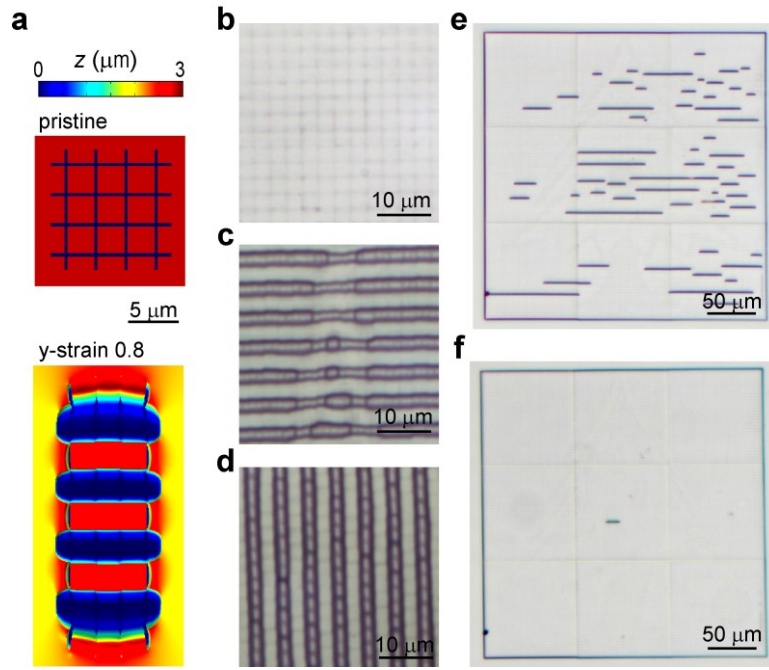


Supplementary Fig. 14 | Top view (a) and 30° tilted view (b) SEM images of the IP-Dip mould for making the PDMS relief with a covert fish image. The area of the dorsal fin is zoomed in. An image of fish with 99×99 pixels is encoded in $297 \times 297 \mu\text{m}^2$ area. Each pixel contains a cuboid with a length

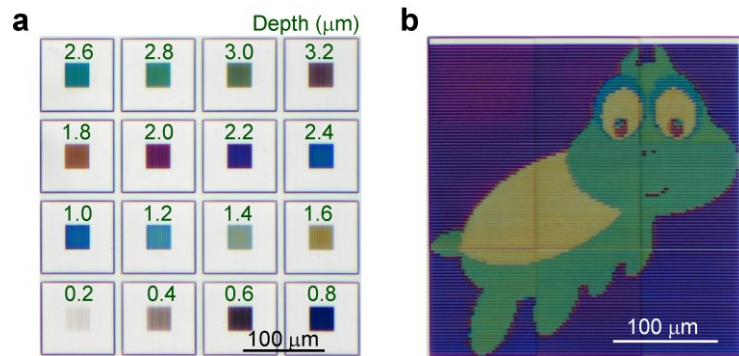
of 3 μm , width of 0.32 μm , and colour-dependent depth. **c**, High-magnified optical images of the fin area with the PDMS trenches at the pristine state (i), loaded with a 0.8 strain along the width direction of the trenches (ii), and at the recovered state (iii).



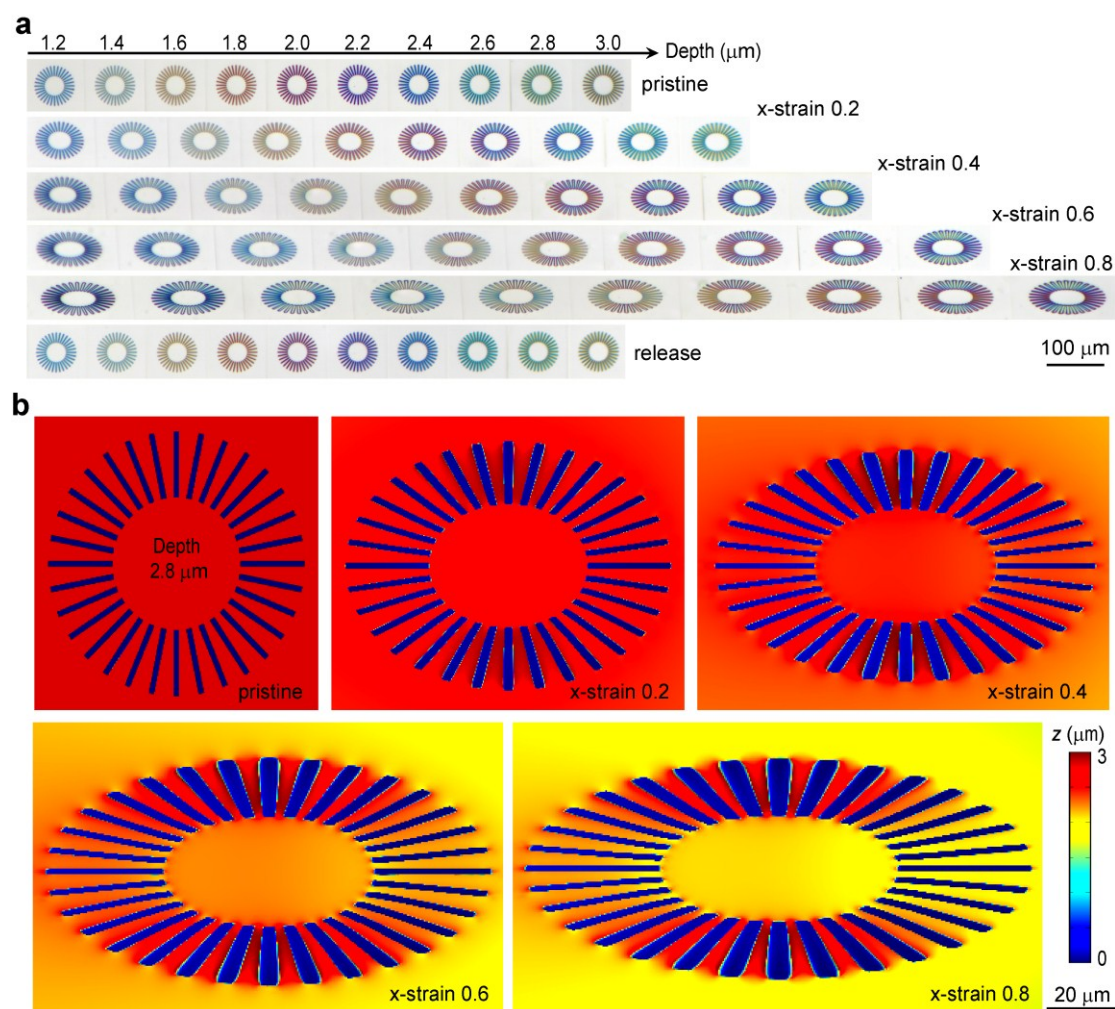
Supplementary Fig. 15 | Transmission optical micrographs of a fish during 200 stretching/releasing cycles. 0.8 strains along the width direction of the trenches are employed and then released for each cycle. Some random lines are observed in the release state, resulting from the residual stress-deformed PDMS trenches. All of the images share the same scale bar.



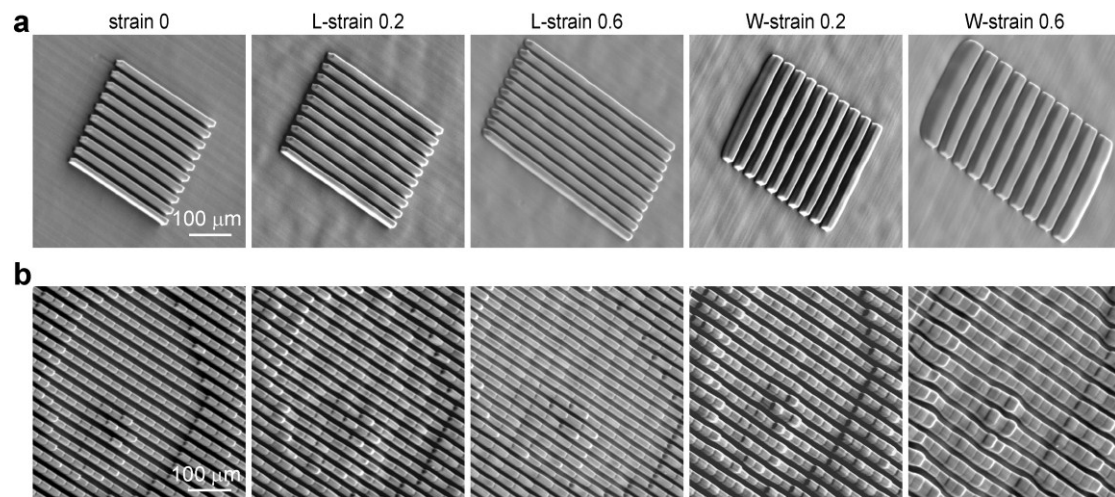
Supplementary Fig. 16 | a, Simulated shape deformation of two orthogonally interlaced PDMS trench arrays. The pristine trench arrays have lengths of 12 μm , widths of 0.32 μm , depths of 2.8 μm , and pitches of 3 μm . When a y-strain is applied, the x-trenches are broadened and the y-trenches are closed. **b-d**, High-magnified optical images of the PDMS trenches (Fig. 5d) at the tip area of the tree. The narrow trenches at the pristine state (**b**) are selectively opened up by the 0.8-strain along either y direction (**c**) or x direction (**d**). **e**, Transmission optical micrograph of the PDMS relief once the 0.8 y-strain is released. Some random lines are observed, which result from the residual stress-deformed PDMS trenches. Most of the lines disappear after keeping the sample undisturbed for 2 h (**f**).



Supplementary Fig. 17 | Transmission optical micrographs of the 10th PDMS replicas moulded from the IP-Dip cuboids. **a**, Colour palette of PDMS trench arrays with depths varying from 0.2 μm to 3.2 μm , lengths of 30 μm , widths of 1.55 μm , and pitches of 3 μm . **b**, Colour image of a turtle.



Supplementary Fig. 18 | **a**, Transmission optical micrograph of radial arrays made of PDMS trenches with varying depths. Each radial array with an outer radius of 36 μm contains 32 PDMS trenches with the same widths of 1.55 μm and lengths of 18 μm , but continuously changing orientation angles at an 11.25° step. The PDMS slab is stretched along the x direction with 0.2, 0.4, 0.6, and 0.8 strains, and then released. **b**, Simulated shape deformations of the radial array of PDMS trenches.



Supplementary Fig. 19 | 30° tilted view SEM images of the Ormostamp replicas moulded from the same PDMS slab with different pre-strains. **a**, A PDMS trench array with a length of 30 μm, width of 1.55 μm, depth of 2.8 μm, and pitch of 3 μm is used as the mould. Ormostamp replicas with different patterns are obtained when different strains are applied to the PDMS mould. All images share the same scale bar. **b**, The turtle in Fig. 3 is used as the mould. The eye areas of the different Ormostamp replicas moulded from the same turtle template with different pre-strains are shown. All images share the same scale bar.